Deciphering Colorectal Cancer-Hepatocyte Interactions: A Multiomic Platform for Interrogation of Metabolic Crosstalk in the Liver-Tumor Microenvironment

Alisa B. Nelson[1], Lyndsay E. Reese[2], Elizabeth Rono[3], Eric D. Queathem[1,4,5], Yinjie Qiu[6], Braedan M. McCluskey[6], Alexandra Crampton[3], Eric Conniff[3], Katherine Cummins[3], Ella Boytim[7], Senali Dansou[3], Justin Hwang[7], Sandra Safo[8], Patrycja Puchalska[1], David K. Wood[3], Kathryn L. Schwertfeger[2,7], Peter A. Crawford[1,3*]

[1]Division of Molecular Medicine, Department of Medicine, University of Minnesota, Minneapolis, MN USA;
[2]Department of Laboratory Medicine and Pathology, University of Minnesota, Minneapolis, MN USA;
[3]Department of Biomedical Engineering, University of Minnesota, Minneapolis, MN USA;
[4]Department of Biochemistry, Molecular Biology, and Biophysics, University of Minnesota, Minneapolis, MN USA;
[5]Department of Integrative Biology and Physiology, University of Minnesota Medical School, Minneapolis, MN, USA;
[6]Minnesota Supercomputing Institute, Minneapolis, MN USA;
[7]Masonic Cancer Center, University of Minnesota, Minneapolis, MN USA;
[8]Division of Biostatistics and Health Data Science, University of Minnesota, Minneapolis, MN, USA

*Corresponding author

Email: crawforp@umn.edu

Author Contributions: ABN, LER, ER, AC, EC, KC, PP, DKW, KLS, PAC: conception and design of the experiments. ABN, LER, EDQ, YQ, BMM, EB, SD, JH, PP, DKW, KLS, PAC: collection, analysis, and interpretation of data. ABN, PP, DKW, KLS, PAC: drafting and revising the manuscript. DKW, KLS, PAC: funding acquisition. All authors have read and approved the final submission.

Competing Interest Statement: P.A.C. has served as an external consultant for Pfizer, Inc., Abbott Laboratories, Janssen Research & Development and Juvenescence.

Keywords: Cancer metabolism, metabolomics, multi-omics, tumor microenvironment

Abstract

Metabolic reprogramming is a hallmark of cancer, enabling tumor cells to adapt to and exploit their microenvironment for sustained growth. The liver is a common site of metastasis, but the interactions between tumor cells and hepatocytes remain poorly understood. In the context of liver metastasis, these interactions play a crucial role in promoting tumor survival and progression. This study leverages multiomics coverage of the microenvironment via liquid chromatography and high-resolution, high-mass accuracy mass spectrometry-based untargeted metabolomics, ^{13}C-stable isotope tracing, and RNA sequencing to uncover the metabolic impact of co-localized primary hepatocytes and a colon adenocarcinoma cell line, SW480, using a 2D co-culture model. Metabolic profiling revealed disrupted Warburg metabolism with an 80% decrease in glucose consumption and 94% decrease in lactate production by hepatocyte-SW480 co-cultures relative to SW480 control cultures. Decreased glucose consumption was coupled with alterations in glutamine and ketone body metabolism, suggesting a possible fuel switch upon co-culturing. Further, integrated multiomic analysis indicates disruptions in metabolic pathways, including nucleoside biosynthesis, amino acids, and TCA cycle, correlate with altered SW480 transcriptional profiles and highlight the importance of oxygen homeostasis in tumor adaptation. Finally, these findings were replicated in 3-dimensional microtissue organoids supporting a bioinformatic approach for studying metabolic crosstalk and discovery of potential therapeutic targets in preclinical models of the tumor microenvironment.

23 **Introduction**

24 The liver is the site of one of six cancers with increasing incidence of primary tumors –
25 hepatocellular carcinoma (hepatoma) (1). Moreover, the liver is a common site of solid
26 tumor cell metastasis, including from breast and colorectal cancers, causing significant
27 morbidity and mortality (2). Tumor cells within the liver interact with liver resident cell types,
28 including hepatocytes. Metabolic adaptation is essential for tumor success throughout
29 cancer cell transformation, proliferation, and metastasis (3, 4). Cancer cells reprogram their
30 metabolism to meet increased demands for energy, biosynthesis, and redox homeostasis.
31 Studies show this adaptation extends to the tumor microenvironment where cancer cells
32 can tune and exploit their environment to meet metabolic needs (5-7). Within the liver,
33 hepatocytes engage dynamic metabolic programs to support local and systemic physiology.
34 Exploitation of this rich metabolic environment may represent an essential interaction that
35 facilitates tumor cell colonization in the liver niche. However, our understanding of the
36 specific interactions between cancer cells and hepatocytes that drive survival and
37 proliferation in the metastatic liver niche remains limited. Previous studies profiling
38 metabolism of HCC indicates transformed hepatocytes engage in aerobic glycolysis and
39 altered lipid and amino acid metabolism (8, 9). Moreover, substrate fuels are used to
40 program neighboring immune cells for repressed anti-tumor responses (7). Metastasizing
41 cells have been shown to require adaptations that help them overcome the hypoxic liver
42 microenvironment (10-12). But these studies do not consider the role of co-localized, non-
43 transformed hepatocytes. Additionally, these studies are limited in their coverage of the
44 omics landscape.

45 Metabolomics technologies are well-positioned to reveal potential metabolic adaptation
46 in cancer. Mass spectrometry-based untargeted metabolomics surveys global metabolic
47 shifts among samples by measuring the fluctuations of multiple chemical feature
48 abundances detected as mass-to-charge (*m/z*) signal and retention time pairs (13-15). An
49 additional dimension of information can be gained by the convergent use of ^{13}C-labeled
50 stable isotope tracers. While static measurement of metabolites provides a snapshot of
51 perturbed influxes or effluxes that lead toward or away from measured metabolites, these
52 measurements often fail to reveal nodes through which shifts occur without significant fold
53 changes in the static abundance of metabolites (16). Merging the advantages of high-
54 resolution mass spectrometry-based untargeted metabolomics with ^{13}C-stable isotope
55 labeling known as isotope tracing untargeted metabolomics (ITUM) provides a unique
56 opportunity to discover dynamic and potentially crucial metabolic pathways (17-20).
57 However, studying metabolic communication in the microenvironment is an ongoing
58 challenge (21). Stable isotopes present an advantage, but developing model systems
59 amenable to ITUM approaches while maintaining physiological relevance is difficult. Here,
60 we present an approach using our untargeted metabolomics and ITUM pipelines in an
61 engineered *in vitro* model to discover metabolic interactions between colon
62 adenocarcinoma cells (SW480 cell line) and primary hepatocytes. To adapt our pipeline to a
63 mixed cell model, we quantify extracellular and intracellular metabolite pools upon co-
64 culture to identify impacted metabolic pathways. Additionally, we hypothesized that the
65 combined study of differential glucose utilization and metabolite-metabolite relationships
66 could reveal tumor cell metabolic adaptation in the hepatocyte-SW480 microenvironment.

67 Therefore, we present approaches that extend the application of untargeted metabolomics
68 and ITUM to reveal nodes of adaptation in the tumor-hepatocyte microenvironment. Finally,
69 a multiomic integration with the transcriptome links metabolic adaptations to altered
70 functional programs in tumor cells with co-localized hepatocytes.
71
72 **Results**
73 **Co-culture of SW480 cells with primary hepatocytes reprograms metabolism.** We used
74 a co-culture model to study metabolic adaptation of tumor cells to the hepatocyte
75 microenvironment. Culturing primary hepatocytes is challenged by their loss of hepatocyte-
76 like function through de-differentiation (22, 23). However, co-culture with 3T3-J2 murine
77 embryonic fibroblasts can sustain hepatocellular function for more than 6 weeks (24).
78 Therefore, we directly co-cultured primary rat hepatocytes, murine 3T3-J2 fibroblasts (J2s),
79 and the human colon adenocarcinoma cell line, SW480 (**Figure 1A**). To form 2D co-cultures,
80 J2s were growth arrested, then plated with hepatocytes in 12-well plates to sustain
81 hepatocellular function (HJ cultures). Control plates of J2s were plated on the same day in
82 preparation for SW480-J2 (SJ) control co-cultures. After 7 days, SW480s were seeded to form
83 SW480-J2-Hepatocyte (SJH) co-cultures and SJ controls. All media and cells were collected
84 on day 10 for metabolomics and transcriptomics analyses (**Figure 1B**). In each experiment,
85 the group of interest, SJH, was compared to HJ and SJ controls.
86 Cancer metabolism is hallmarked by high glucose consumption and utilization through
87 aerobic glycolysis, resulting in high lactate production, known as the Warburg Effect (25, 26).
88 Hepatocytes play significant roles in regulating glucose homeostasis. We hypothesized that

89 hepatocytes may impact glucose metabolism in co-cultures. Therefore, we quantified net
90 changes in glucose and lactate concentrations in conditioned cell culture media using ^{1}H-
91 nuclear magnetic resonance (NMR) spectroscopy. Then, we normalized changes in
92 exogenous metabolite concentrations to cellular biomass (DNA content) to report net
93 glucose consumption and lactate production over 24 hours. As expected, SJ controls model
94 the Warburg effect in culture, consuming 2.50 ± 0.01 mol glucose/day/mg DNA, and
95 producing 3.86 ± 0.05 mol lactate/day/mg DNA (**Figure 2A**). The presence of hepatocytes
96 decreased total glucose consumption by 80% (0.5 ± 0.05 mol glucose/day/mg DNA) and
97 lactate production by 94% to 0.23 ± 0.01 mol lactate/day/mg DNA. Furthermore, the ratio of
98 lactate to glucose significantly decreased from 1.54 ± 0.02 to 0.46 ± 0.05, suggesting the
99 presence of hepatocytes disrupts Warburg metabolism of SW480s (**Figure 2B**).

100 To determine if decreased utilization of glucose by SW480 cells when co-cultured with
101 hepatocytes could result from a fuel switch from glucose to other available substrates, we
102 quantified hepatocyte-derived ketones and culture media-derived glutamine. Using a
103 UHPLC-MS/MS based approach, we quantified total ketone bodies in the conditioned media
104 of co-cultures after 24 hours. As expected, primary rat hepatocyte control co-cultures
105 produced the ketone bodies acetoacetate (AcAc) and β-hydroxybutyrate (βOHB, **Figure 2C**).
106 In the presence of SW480s, total ketone bodies recovered in the media were diminished by
107 64%, suggesting either decreased production by hepatocytes or increased consumption of
108 ketones by non-hepatocyte cells. Glutamine abundance was also significantly decreased in
109 SJH co-cultures relative to both HJ and SJ controls (**Figure 2D**). Interestingly, glutamine
110 abundance decreased 36% in SJH relative to SJ controls, suggesting the presence of

111 hepatocytes further enhanced glutamine dependence of SW480s. Together these data
112 suggest an adaptation to fuel utilization in hepatocyte-SW480 co-cultures.

113 To survey metabolic interaction-dependent metabolite shifts resulting from co-culture,
114 we next used differential analysis of features detected by LC-MS-based label-free
115 untargeted metabolomics. Prior to any downstream analysis, low variance features were
116 removed, features of interest were annotated in Compound Discoverer 3.3, and when
117 possible, matched to commercial standards and MS/MS spectral libraries. Five metabolic
118 features by LC-MS-based untargeted profiling increased more than 2-fold ($\log_2 \geq 1$) in SJH
119 compared to HJ controls. This included putative S-adenosylhomocysteine (SAH; **Table 1,**
120 **Figure 2E**), an intermediate of one-carbon metabolism. Compared to HJ, SJH co-cultures
121 showed 142 downregulated features, including pyruvate (**Supplemental Figure 1A**), acetyl-
122 CoA (**Supplemental Figure 1B**), and propionyl-CoA (**Supplemental Figure 1C**), metabolites
123 important in glucose metabolism and the TCA cycle. Relative to SJ controls, SJH co-cultures
124 show a greater than 2-fold increase in 10 features, including propionyl-CoA (**Figure 2F;**
125 **Supplemental Figure 1C**), glutamyl-glycine, an intermediate of glutathione metabolism,
126 and acetyl-CoA (**Supplemental Figure 1B**). A ≥2-fold decrease was observed in 119 features
127 in SJH compared to SJ controls, including pyruvate (**Supplemental Figure 1A**), lactate
128 (**Supplemental Figure 1D**), NAD^+ (**Supplemental Figure 1E**), and ATP (**Supplemental**
129 **Figure 1F**). However, decreases in the NAD^+ pool did not lead to a significant change in the
130 NAD^+/NADH ratio in SJH relative to SJ (**Supplemental Figure 1G**). Finally, we calculated
131 energy charge to determine the current energy status of the co-culture based on relative
132 abundance of AMP, ADP, and ATP pools. We saw a modest, but not statistically significant,

133 decrease in SJH relative to SJ co-cultures, suggesting a possible decrease in available energy
134 (**Supplemental Figure 1H-I**).
135 Untargeted metabolomics of mixed cell populations represent metabolite pools that are
136 combined across all cell types. Therefore, changes in relative abundance may represent an
137 adaptation in one cell type, a combination of adaptations across multiple cell types, or could
138 simply be a product of dilution of the pool after adding biomass. Due to the observed number
139 of features that were significantly decreased in SJH relative to either HJ or SJ controls, we
140 sought to determine if our approach detects true biological interactions in hepatocyte and
141 SW480 co-cultures, rather than simple dilutions of HJ or SJ metabolite pools. Therefore, we
142 implemented a dilution approach to identify those features that were significantly different
143 from a HJ-SJ dilution (**Figure 3A**). HJ and SJ extracts were combined 1:1 (1T1) prior to LC-MS
144 injection, alongside HJ, SJ, and SJH samples. Putative metabolites with pool sizes that
145 significantly differed between SJH and controls were compared to the 1T1 dilution sample.
146 A low threshold for discovery was used ($p < 0.05$) to identify those features that may indicate
147 metabolic interactions. Lactate, a metabolite known to have altered production in cancer,
148 was significantly decreased in SJH relative to 1T1 samples (**Figure 3B; Table 2**). Normalized
149 ion counts for each group and the analytical control, 1T1, are shown in **Supplemental Figure**
150 **2**, demonstrating a likely metabolic interaction between SW480s and hepatocytes beyond
151 an outcome that could be explained by simple metabolite pool dilution. Additionally, four
152 glutamyl peptides – including glutamyl-glycine, as well as uracil, uridine diphosphate (UDP),
153 aspartate, and malate were increased more than 2-fold in SJH relative to 1T1 (**Figure 3B;**
154 **Table 2**). Employment of an analytical 1T1 dilution of controls for differential analysis of

155 directly co-cultured cells reveals biological derangement of metabolite abundances
156 belonging to glycolytic, amino acid, and nucleoside pathways.

157 **Metabolite exchange of nucleoside intermediates.** Untargeted metabolomics results
158 indicate altered activity in both purine and pyrimidine pathways when SW480s are co-
159 cultured with hepatocytes, whose identities were confirmed by retention time and MS/MS
160 fragmentation match to commercial standards (**Figure 2E-F; Figure 3B**). We hypothesized
161 that the presence of hepatocytes may facilitate adaptation through exchange of purine and
162 pyrimidine intermediates. Therefore, we performed LC-MS-based untargeted metabolomics
163 on cell extracts and media after the first 24 hours of direct co-culture to evaluate fold
164 changes in nucleoside intermediate abundance over time. In all three groups, hypoxanthine,
165 an intermediate of purine metabolism, was depleted comparing starting media (t0) to media
166 harvested after 24 hours, indicating uptake from serum-containing media or conversion to
167 other metabolic products (**Figure 4A, Table 3**). SJH co-cultures had 23% (±3%) greater
168 depletion of hypoxanthine compared to HJ controls and 12% (±4%) less than SJ controls
169 (**Supplemental Figure 3**). Interestingly, hypoxanthine abundance was coupled with
170 diminished extracellular uric acid, the terminal product of purine degradation, in HJ and SJH
171 groups, while SJ controls show an average 809% increase in uric acid (**Figure 4A,**
172 **Supplemental Figure 3**). Hypoxanthine and uric acid are both metabolites that can be found
173 in starting media due to the presence of serum. We further analyzed media under normal
174 culture conditions and in the absence of cells to control for possible spontaneous
175 degradation and observed an accumulation of hypoxanthine and uric acid (9% and 47%,
176 respectively) after 24 hours, suggesting instability of upstream metabolites at 37°C (denoted

177 as dotted lines, **Supplemental Figure 3**). Therefore, these data indicate significant
178 metabolic activity in the purine degradation pathway in SJ controls that is altered by the
179 presence of hepatocytes. To investigate if this impacts intracellular purine intermediates, we
180 measured inosine in cellular extracts. Inosine, an intermediate in the purine salvage
181 pathway, showed a 2-fold increase in hepatocyte-containing cultures while it was modestly
182 diminished in SJ controls after 24 hours (**Figure 4B**). Finally, inosine was uniquely enriched
183 from [U-$^{13}C_6$]glucose in HJ and SJH groups but not detectable in SJ in 3D microtissue
184 organoids (**Figure 4C**). Conversely, the average total ^{13}C-enrichment of HJ and SJH groups
185 was 58.7% (± 1.5%) and 64.7% (± 4.5%) of the total inosine pool. This observation suggests
186 that changes in glucose contribution to inosine pools may be localized to hepatocytes.
187 Together these data suggest the presence of hepatocytes increases purine salvage, rescuing
188 cells from uric acid accumulation.
189 *Pyrimidine metabolism is increased in hepatocytes by co-culture with SW480 cells*.
190 Hepatocytes are a primary source of uridine, an intermediate of pyrimidine metabolism. We
191 hypothesized that altered pyrimidine pools may be a result of newly available uridine from
192 hepatocytes. Therefore, we measured pyrimidine intermediates by LC-MS/MS in media and
193 cell extracts to observe changes in pool sizes over 24 hours compared to starting media. As
194 expected, we observed an accumulation of uridine in the media of hepatocyte-containing
195 co-cultures that was not present in SJ controls (**Figure 4D**). Interestingly, we observed an
196 even greater accumulation of orotic acid, an intermediate of *de novo* pyrimidine
197 biosynthesis (**Table 3**). We did not observe a significant difference between SJH and HJ
198 controls, suggesting these media signals are primarily driven by hepatocytes. However,

199 intracellular pool sizes of pyrimidine metabolites showed greater increases in SJH relative to
200 HJ controls, including carbamoyl aspartate – the product of the rate-limiting step in *de novo*
201 pyrimidine biosynthesis, suggesting the co-localization of hepatocytes and SW480s
202 upregulates the pyrimidine biosynthetic pathway (**Figure 4E**).

203 **Discriminant ^{13}C-ITUM analysis of SJH co-cultures.** ^{13}C-stable isotope tracing of
204 metabolic substrates has been used to detect metabolic adaptation (19, 27). However,
205 incorporation of glucose-derived carbon in diverse metabolic pathways in mammalian cells
206 convolutes biological interpretation of enrichment patterns in complex samples. We
207 hypothesized that informatic integration of co-^{13}C-enriched metabolites elucidates pathway
208 activity. Therefore, we employed univariate and multivariate statistical approaches to
209 characterize glucose utilization in co-culture. SJ and SJH co-cultures were treated with [U-
210 $^{13}C_6$]-glucose for 24 hours on day 9. On day 10, cells were snap frozen for ^{13}C-ITUM and
211 acquired LC-MS data was analyzed for ^{13}C-enriched mass isotopomers (*i.e.,* isotopologues)
212 [M+0, M+1, ..., M+n] to identify nodes of glucose-derived metabolism that differentiate SJH
213 co-cultures from SJ controls. We first used principal components analysis (PCA) to identify
214 isotopologues that discriminate SJH co-cultures from HJ and SJ controls (**Figure 5A**). PC1
215 significantly separated SJH and SJ groups, while PC2 moderately separated SJH from HJ
216 controls. Strong association with PC1 indicated co-^{13}C-enrichment of these metabolites
217 captures the impact of hepatocytes on SW480s. To further investigate adaptations to
218 glucose metabolism after co-culturing hepatocytes on SW480s, we performed a univariate
219 correlation analysis of top contributors to PC1 loadings, including only SJ and SJH ^{13}C-
220 enrichment. We visualized these relationships in a correlation matrix (**Figure 5B;**

221 **Supplemental Figure 4**). A positive correlation between feature pairs indicates co-^{13}C-
222 enrichment of isotopologue pools in response to SW480 co-culture with hepatocytes
223 relative to SW480 alone, while a negative correlation indicates a possible bifurcation of ^{13}C-
224 labeled carbon because of co-culture. As would be expected, fractional enrichment of M+0,
225 the isotopologue indicating no ^{13}C incorporation, of several metabolites, including TCA cycle
226 intermediates, were positively associated with each other and clustered together ("Region
227 1" on **Figure 5B**). These M+0 species show a strong negative correlation with the ^{13}C-
228 enriched isotopologues (species in "Region 2"), *e.g.*, M+0 of Glutamate ("E_M0") versus the
229 incorporation of four ^{13}C atoms ("E_M4"). This is the expected relationship and supports the
230 validity of this analytical framework, which also reveals many unanticipated relationships.
231 For example, the M+6 isotopologue of uridine diphosphate N-acetylglucosamine
232 (UDPGlcNAc, corresponding to the direct incorporation of a labeled glucose molecule into
233 glucosamine), clustered with unenriched (M+0) isotopologues of several metabolites in
234 Region 1 (Red arrow, **Figure 5B**) and negatively correlated with enriched glutathione (*e.g.*,
235 GSH_M3, found in Region 2; Blue arrow). UDPGlcNAc M+6 enrichment decreases in co-
236 culture, while enrichment of GSH increases (relative to the SJ condition), suggesting glucose
237 is redirected from the hexosamine biosynthetic pathway to glutathione synthesis in co-
238 culture (**Supplemental Figure 5**). Region 3 shows a cluster of isotopologues from glycolytic
239 and TCA cycle intermediates with strong co-enrichment. As expected, this includes
240 enriched isotopologues of metabolites in the same pathway, such as glutamate (E_M4), a
241 precursor to GSH (GSH_M4; Yellow arrows, **Figure 5B**). The positive co-enrichment of other
242 TCA cycle intermediates with GSH may meet GSH demand in response to co-culture. Finally,

243 Region 4 shows isotopologues with nominal relationships to each other, suggesting little
244 change in response to co-culture. Together these data indicate ^{13}C-enrichment of
245 glutathione from glucose is significantly impacted by co-culturing of SW480s and
246 hepatocytes. Glutathione is an important metabolite in redox homeostasis within the cell
247 and changes to its biosynthesis may be a significant adaptation of metabolic pathways to
248 the tumor-hepatocyte microenvironment.

249 **Transcriptomic analysis of 3-dimensional hepatocyte-SW480 microtissue organoids.** To
250 evaluate SW480 adaptation to co-culturing with hepatocytes in a more physiological setting,
251 we also performed transcriptomic profiling of SJ and SJH groups using a 3D microtissue
252 organoid model. We co-cultured SW480 with primary rat hepatocytes and 3T3-J2 fibroblasts
253 within collagen I-based microtissues (**Figure 6A**). Conditions included SJ cells and SJH using
254 the same cell numbers and proportions as 2D co-culture. The SJH tricultures alongside co-
255 culture controls were maintained for 7 days before harvesting for transcriptional and
256 metabolic analyses. To identify transcriptional alterations that occur in cancer cells upon
257 exposure to hepatocytes, we performed bead isolation using antibodies against CD326
258 (EpCAM) to isolate the SW480 tumor cells grown in the presence and absence of
259 hepatocytes and supporting J2s and performed bulk RNA-seq analysis to identify genes and
260 pathways that are modulated when exposed to hepatocytes. We found that exposure of
261 tumor cells to hepatocytes led to increased expression of 708 genes and decreased
262 expression of 762 genes in SW480 cells (adj. $p < 0.05$) (**Figure 6B**). Further analysis of gene
263 ontology (GO) and gene set enrichment analysis (GSEA) demonstrated significant
264 alterations in hallmark pathways of Myc targets and pathways associated with several

265 metabolic processes, including oxidative phosphorylation, metabolism of amino acids, GSH
266 metabolism, and fatty acid metabolism (**Figure 6C-E; Supplemental Table 1,2**). We also
267 compared RNAseq findings to oncogenic pathways (**Figure 6F**). These findings demonstrate
268 that hepatocytes drive transcriptional changes in tumor cells, many of which are associated
269 with changes in metabolic pathways.

270 **Multiomics analysis of differentially expressed genes and static metabolite pools.** Our
271 2D co-culture metabolomics pipeline and 3D transcriptional profiling both identified
272 adaptations in amino acid, biosynthetic, and oxidative pathways. Therefore, we integrated
273 these datasets in 2D to identify metabolite-gene relationships important to the SW480-
274 hepatocyte microenvironment. Multiomic integration of a tumor cell transcription profile
275 and metabolomic datasets can help establish the relationship between bulk metabolic
276 adaptation and tumor cell phenotype. After bead isolation from hepatocytes and 3T3-J2s
277 using antibodies against CD326 (EpCAM), RNA from SW480s was isolated and sequenced.
278 Differentially expressed genes (adj. $p < 0.01$) were combined with significantly altered
279 metabolite pools (**Figure 3B**) for univariate association analysis, recovering 627 mRNAs that
280 were significantly correlated with 255 putative metabolites ($p < 0.001$, **Supplemental Table**
281 **3**). We further filtered this correlation matrix to only include very strong associations ($R >$
282 $|0.98|$) to identify a subset of genes related to metabolic adaptation. A total of 151 unique
283 genes correlated strongly with lactate, orotic acid, glutamyl-glycine (glu-gly), malate, and
284 UMP (**Figure 7A**). In these analyses, positive correlations indicate co-expression in response
285 to co-culture while negative correlations indicate opposing expression pattern in response
286 to co-culture. Given our findings of glutathione metabolism, we chose to look closer at the

287 98 genes that associated with the metabolite glutamyl-glycine for gene-gene relationships
288 (**Figure 7B**). GO enrichment analysis of biological processes of 98 genes associated with glu-
289 gly revealed enrichment regulation of the cell cycle, response to hypoxia, and tissue
290 morphogenesis (**Figure 7C**). Ontologies associated with all 151 genes further included
291 adhesion, hypoxia, and angiogenesis (**Supplemental Figure 6A-B**).

292 In this study we have demonstrated a multiomic platform that uses LC-MS-based
293 untargeted metabolomics approaches and bulk RNA-sequencing to reveal complex
294 interactions in a mixed cell population. Additionally, these approaches can be translated to
295 3D microtissue organoid models. Bioinformatic interrogation of datasets suggests an
296 important adaptation to changing oxygen environment and ROS management occurs in the
297 tumor microenvironment upon introduction to hepatocytes.

298

299 **Discussion**

300 This study employed a multiomic approach to uncover metabolic adaptation in the tumor-
301 hepatocyte microenvironment using co-cultures of human colon adenocarcinoma cells
302 (SW480) and primary rat hepatocytes, with the support of murine 3T3-J2 fibroblasts. By
303 integrating untargeted metabolomics, ^{13}C-stable isotope tracing untargeted metabolomics
304 (ITUM), and transcriptomic analysis, we identified several critical metabolic alterations
305 driven by the interaction between tumor cells and hepatocytes. First, co-culture of SW480s
306 with primary hepatocytes significantly altered glucose metabolism. Hepatocytes reduced
307 glucose consumption by 80% and lactate production by 94%, compared to SW480
308 monocultures. This suggests hepatocytes disrupt the classical Warburg effect in SW480

309 cells by influencing glucose metabolism (4, 26, 28). Previous work indicates that aerobic
310 glycolysis is an important adaptation for overcoming hypoxia within the liver, thus
311 suppression by hepatocytes may impact survival (10). Hepatocytes display highly dynamic
312 metabolism that serves to regulate glucose homeostasis. In the presence of high glucose
313 levels, hepatocytes can direct excess glucose molecules to storage as glycogen, *de novo*
314 lipogenesis, or to produce uridine (29). Additionally, hepatocytes can use alternative
315 substrates, such as lactate, for glucose production. These dynamic, yet somewhat
316 opposing, metabolic programs may be impacted by the presence of lactate-producing
317 SW480s and lead to the altered glucose metabolism observed in these experiments. Further
318 study is necessary to deconvolute these substrate fluxes.

319 In response to reduced glucose consumption, SW480 cells adapted their fuel utilization.
320 We observed a substantial reduction in ketone bodies and glutamine in the media of co-
321 cultures, indicating increased consumption of these alternative substrates. In absence of
322 glucose, tumor cells can reportedly shift to alternative fuels, such as glutamine, however
323 whether this plasticity extends to ketone bodies is not yet well understood. Ketogenesis has
324 been a topic of interest in cancer research (30). Studies have indicated a relationship
325 between diminished expression of rate-limiting enzyme, 3-hydroxy-3-methylglutaryl
326 synthase 2 (HMGCS2), and tumorigenesis (31-33). Thus, it is also possible diminished
327 ketones in the media is due to reduced production through ketogenesis. Further, targeting
328 ketogenesis has been proposed as a potential therapeutic strategy for inhibiting tumor
329 progression, though responses *in vivo* vary between cancer types and stages (30, 34-37).
330 Suggesting the impact of the SW480-hepatocyte interaction on ketone body metabolism

331 may represent adaptation for tumor survival. As ketogenic capacity has also been shown to
332 vary across the spectrum of metabolic dysfunction-associated steatotic liver disease
333 (MASLD), further study of the relationship between ketogenesis, cancer, and liver health is
334 warranted.

335 Untargeted metabolomics revealed additional changes in metabolites associated with
336 the TCA cycle and energy metabolism. Notably, acetyl-CoA was elevated, while pyruvate,
337 ATP, and NAD^+ were decreased, highlighting key metabolic nodes affected by hepatocyte
338 presence. The co-culture system revealed a possible metabolic exchange between
339 hepatocytes and SW480 cells, particularly in purine and pyrimidine metabolism. SW480s in
340 co-culture displayed enhanced salvage and reduced uric acid production, coupled with
341 increased pyrimidine biosynthesis. Uric acid can regulate oxidative stress, activity of
342 enzymes related to glucose metabolism, and is associated with development of metabolic
343 syndrome (38). Additionally, uric acid is linked with cancer risk (39, 40). Therefore, the
344 modulation of uric acid levels and purine metabolism may be critical for targeting tumor
345 growth. Further, due to comorbidities of cancer and obesity, the intersection of uric acid and
346 metabolic syndrome in the tumor-hepatocyte niche may be an important area of further
347 study. Recent work has established the pyrimidine intermediate, uridine, as an alternative
348 fuel source for cancer cells in a glucose restricted environment (41, 42). As uridine was
349 elevated in the media of hepatocyte-containing cultures, it is possible SW480s utilize this
350 metabolite to drive activity in the pyrimidine pathway. Further study is needed to understand
351 how access to uridine impacts cancer metabolism in the liver and how flux through these
352 nucleoside pathways may impact the oxidative environment.

353 ^{13}C-stable isotope tracing of mixed cell populations results in convoluted ^{13}C-enrichment
354 datasets that can be difficult to interpret for individual cell populations. For this reason,
355 studies often employ conditioned media exchange to study intercellular metabolic
356 dependencies. These studies are limited by the lack of cellular contact that may be relevant
357 to metabolic interactions and the difficulty adapting these methods toward the more
358 complex and advantageous preclinical models of the microenvironment, such as 3D
359 microtissue organoids. Using unsupervised dimension reduction and association analyses,
360 discriminant ^{13}C-ITUM allows for pathway analysis by identifying 1) enriched isotopologues
361 that discriminate groups and 2) metabolite-metabolite relationships within the
362 discriminating isotopologue set. Therefore, discriminant ^{13}C-ITUM is a form of pathway
363 analysis that highlights co-enriched metabolic pathways characterizing mixed cell
364 populations. This systems-level approach enables specificity to substrate utilization with
365 fewer constraints than metabolic flux analysis.

366 Transcriptomic profiling of SW480s revealed adaptation to metabolic pathways and
367 enrichment of oncogenic pathways, including YAP, PTEN, and MYC. These signaling hubs
368 have been implicated in the regulation of cancer cell metabolism (43-45). Here we observe
369 their regulation in response to the presence of hepatocytes in the tumor microenvironment.
370 Multiomic integration of metabolomics and RNA-seq data further showed that metabolic
371 adaptations were associated with significant transcriptional changes in SW480 cells. These
372 changes were linked to key biological processes, including adhesion, hypoxia response, and
373 angiogenesis, indicating that tumor cells undergo functional adaptation in response to the
374 hepatocyte microenvironment. These results are further supported by co-enrichment

375 networks through a novel analysis of ITUM datasets, which we have called discriminant
376 ITUM. This analysis indicated the importance of glutathione synthesis in differentiating
377 SW480-hepatocyte co-cultures from SW480 controls. Finally, these findings were supported
378 by preliminary studies of a 3D microtissue organoid model, which demonstrated that co-
379 culturing SW480 cells with hepatocytes induces similar transcriptional and metabolic
380 changes observed in 2D co-culture system.

381 While this study provides important insights into the metabolic interplay between tumor
382 cells and hepatocytes, several limitations should be acknowledged. First, the use of 2D co-
383 cultures, though effective in revealing key metabolic interactions, lacks the complexity of *in*
384 *vivo* systems and may not fully capture the spatial and structural dynamics present in the
385 liver microenvironment. Future work in advanced models such as organ-on-a-chip or 3D
386 culture systems could provide more physiologically relevant insights. Additionally, our
387 analysis primarily focused on the metabolic and transcriptional changes in tumor cells,
388 leaving the metabolic impact on hepatocytes underexplored. Future work should involve a
389 comprehensive assessment of hepatocyte responses to tumor interaction, including
390 potential metabolic reprogramming. Mechanistic studies targeting the identified metabolic
391 nodes, such as altered glucose and ketone metabolism or nucleoside exchange, could
392 further elucidate their roles in tumor progression and present potential therapeutic
393 strategies to disrupt these metabolic dependencies.

394

395 **Materials and Methods**

396 *Reagents*

397 LCMS grade water (H2O) (Fisher, W6-4), LCMS grade methanol (MeOH) (Fisher, A456-4),
398 LCMS grade acetonitrile (ACN) (Fisher, A955-4), DMEM (high glucose) (Thermo, 11965092),
399 DMEM (no glucose) (Thermo, A1443001), fetal bovine serum (Biotechne, S11150), Pen/Strep
400 (Thermo, 15140122), L-glutamine (200 mM) (Thermo, 25030081), Phosphate Buffered Saline
401 (PBS) (no CaCl2 or MgCl2) (Thermo, 14190144), Molecular Biology Grade Water (Corning,
402 46-000-CM), Pierce BCA Protein Assay Kit (Thermo, 23225), Genomic DNA kit (blood and
403 cultured cells) (IBI scientific, IB47201). 0.25% Trypsin-EDTA (Corning 25-053-Cl), Hank's
404 Balanced Salt Solution (HBSS) (with CaCl2 or MgCl2) (Gibco 14025-076), Collagenase Type
405 IV (Sigma Aldrich, C5138), Human CD326 (EpCAM) MicroBeads (Miltenyi Biotec, 130-061-
406 101), CD16/CD32 Monoclonal Antibody (Invitrogen 14-0161-82), LS Magnetic Separation
407 Columns (Miltenyi Biotec 130-042-401), QuadroMACS Magnetic Separator (Miltenyi Biotec
408 130-090-976), RNeasy Mini Kit (Qiagen, 74104).

409

410 *2D and 3D culture platform*

411 For both 2D and 3D cultures, 3T3-J2 fibroblasts (Kerafast, Catalog Number: EF3003) and
412 SW480 cells (ATCC, lot Number: 700031955) are maintained in tissue culture flasks until
413 ready for use. Primary rat hepatocytes (PRH, Cryopreserved Male Wistar Rat Plateable
414 Hepatocytes AMY 7 mil, Catalog Number: r3000.H15 Lot No. 1210326) were thawed
415 immediately before use. 3T3-J2 fibroblasts are growth arrested using 1 μg/mL mitomycin-C
416 for 4 hours in culture before detachment using trypsin-EDTA.

417 In 2D, 150k PRH and 150k 3T3-J2 fibroblasts are plated per well for all HJ, SJH, SJ wells.
418 On day 7, 50k SW480 cells are seeded to SJH and SJ wells. On day 9, cell culture media is

419 changed to exchange equimolar (22 mM) unlabeled glucose for non-radioactive, stable
420 isotopically labeled 22 mM [U-$^{13}C_6$]glucose according to previously established protocols
421 (46). Cells and final conditioned media are collected on day 10.

422 3D microtissue organoids were fabricated as previously described (24). Briefly, plates
423 were with 2% agarose and allowed to stiffen for 24 hours. We then used a microwell stamp
424 made from a PDMS mold to create 200 μM microwells that held the microtissues separately
425 within the same well. After cleaning the microwells with a series of washes, we added media
426 to the wells. We maintained the microtissues in Human Hepatocyte Maintenance Media
427 (HHM) (43.25mL 1x DMEM, 5 mL Bovine Serum, 750 μL HEPES, 1M, pH 7.6, 500 μL
428 insulin/human transferring/selenous acid and linoleic acid premix (Corning premix
429 solution), 500 μL Penicillin-streptomycin, 100X solution of 50 mg/mL stock, 0.5 μL
430 Dexamethasone, 10 mM in DMSO, 0.5 μL Glucagon, 0.7 mg/mL in 0.05 M acetic acid. During
431 the study, we provided fresh media changes every 48 hours by removing 300 μL from each
432 well and replacing it with 300 μL of fresh media. We then removed the microtissues at their
433 respective time point.

434 *Quantification of Glucose and Lactate via 1 H NMR*

435 ~50 μL of cell culture media was dried to completion in a SpeedVac in the presence of D_2O
436 to aid in water suppression. Samples were reconstituted in D_2O (99.9%) spiked with 0.3 mM
437 d_4-trimethyl-silyl propionate (TSP). ^{1}H-NMR signals were acquired using a Bruker Avance III
438 600 NMR instrument equipped with a CryoProbe, then the integrated intensities of the α-
439 anomeric proton on glucose carbon-1, the methyl signal for lactate, and the tri-methyl signal

440 from TSP, were used to calculate molar concentrations of the respective substrates. For all
441 ^{1}H-NMR collections, spectra were collected by conventional pulse-and-collect
442 measurements under quantitative conditions (10-ppm spectral range using ~15 μs [90°]
443 excitation pulse and 22-second delay between each of 20 transients).

444 *Untargeted Metabolomics and Isotope Tracing Untargeted Metabolomics pipeline*

445 Cells are harvested, metabolites extracted, and raw data acquired using liquid
446 chromatography (LC) on a Thermo Vanquish UHPLC system, and full-scan high-resolution
447 mass spectrometry (HR-MS) on a Thermo QExactive plus hybrid quadrupole-orbitrap mass
448 spectrometer fitted with heated electrospray ionization source and operated in negative and
449 positive polarity mode.

450 **Cell collection for metabolomics.** Media was collected and snap frozen, then adherent
451 cells were washed twice with 1 mL warm (37°C) PBS (-MgCl2, -CaCl2), once with warm
452 (37°C) cell-culture grade H2O, then the entire plate was submerged into liquid nitrogen to
453 snap freeze cells, which rapidly quenches metabolism. To preserve the metabolome, cells
454 were scraped in 500 μL of cold (-20°C) LCMS grade MeOH per well of cells. Two wells were
455 combined to form each replicate, n = 3 per group. Finally, MeOH was evaporated using a
456 SpeedVac. Dried cell pellets were stored at -80°C until analysis.

457 **Metabolite extraction.** Metabolites from cell pellets and conditioned media were
458 extracted and analyzed by LC-MS untargeted metabolomics according to previously
459 published protocols (46, 47). Briefly, cell pellets are reconstituted in 1 mL 2:2:1 (v/v/v)
460 ACN:MeOH:Water, then vortexed (30s), flash frozen in liquid nitrogen (1 min), and sonicated
461 (25°C, 10 min) in three cycles. After 1 hour at -20°C, samples are centrifuged at 15k x g at 4°C

462 for 10 minutes. Supernatant was transferred to a fresh tube and dried by SpeedVac
463 overnight, while the remaining cell pellet was stored at -80°C after removing any remaining
464 solvent for DNA quantification. Cell extracts are reconstituted in 40 µL 1:1 (v/v) ACN:Water
465 for analysis. 20 µL of conditioned media was extracted in 80 µL 1:1 (v/v) ACN:MeOH. Media
466 underwent a single cycle of vortex and sonication, then followed the same procedure as cell
467 pellets. Media samples were reconstituted in 200 µL 1:1 (v/v) ACN:Water for analysis.

468 **Data acquisition.** For this study, polar metabolites were acquired using hydrophilic
469 interaction chromatography (HILIC) and energy nucleotides were acquired by reverse phase
470 (RP), using two unique UHPLC methods: **[1]** SeQuant ZIC-pHILIC column (2.1 x 150 mm, 5
471 µm) (Millipore Sigma, 1.50460). Mobile phase A (MPA) was 95% H2O, 5% ACN, 10 mM
472 ammonium acetate, and 10 mM ammonium hydroxide. Mobile phase B (MPB) was 100%
473 ACN. The total run time was 50 minutes, flow rate was 2 mL/min, column chamber was set
474 to 45°C, and 2 µL sample was injected. Mobile phase gradient was as follows: 0-0.5 min,
475 90% MPB; 0.5-30 min, 90→30% MPB; 30-31 min, 30% MPB; 31-32 min, 30→0% MPB; 32-33
476 min, 0→90% MPB; 33-50 min, 90% MPB. **[2]** Energy nucleotides (ATP, ADP and AMP), and
477 redox nucleotides (NAD^+ and NADH) were measured as previously described, with
478 modifications. Briefly, metabolites were extracted from cells for ITUM in MeOH:ACN:H2O
479 (2:2:1), then extracts were separated and detected using ion-pairing RP UHPLC-MS/MS on a
480 C18 column (Waters Xbridge, 150 x 2.1mm, 3µm). Nucleotides were detected as adducts of
481 dibutylamine acetate on a Thermo QExactive Plus mass spectrometer, operated in positive
482 ionization mode, using parallel reaction monitoring transitions as previously described.

483 For all metabolomics pipelines, both blanks and pooled quality control (QC) samples are
484 injected periodically throughout the run. Blanks were ACN:H2O (1:1) and the QC sample was
485 a pooled sample including all naturally-occurring and ^{13}C-labeled samples. To aid in
486 chemical feature identification, two additional samples were also injected. First, was a
487 standard mix consisting of authentic standards, for all expected analytes. Second, was a
488 pooled sample consisting only of the naturally-occurring samples, analyzed via data-
489 dependent analysis (DDA) tandem mass spectrometry (MS/MS) using IE omics script and R-
490 Studio (48).

491 **Data preparation.** Data processing and initial analysis was performed using Thermo
492 Compound Discoverer 3.3. After raw mass spectra were uploaded, background ions were
493 removed, retention time (RT) for detected signals were aligned across samples, chemical
494 formulas were predicted, then grouped chemical features were profiled to determine
495 compound identity, based on (1) the m/z predicted from the chemical formula, (2) the RT
496 compared to an authentic external standard, and (3) the MS/MS fragmentation pattern,
497 compared to in-house standards or online databases.

498 For ITUM experiments, putatively identified metabolites and lipids were then carried
499 forward and [^{13}C] stable-isotope enrichment with correction for natural abundance. To carry
500 out [^{13}C] stable isotope tracing, all [^{13}C] mass isotopomers (*i.e.,* isotopologues) within the
501 isotopic envelope of each identified metabolic pool were identified based on the diagnostic
502 shift in m/z ($\Delta m/z$ = 1.0033 Da, natural abundance, 1.11% of all carbon) induced by the
503 presence of ^{13}C-labeled compounds. Raw ion counts for each isotopologue were extracted,
504 summed, and expressed as a percentage of the total pool. After natural abundance

505 correction, the fractional intensities were then graphed as a function of [^{13}C] content,
506 generating mass isotopologue distributions (MIDs) for each detected metabolite or lipid.
507 For static pool analysis, total ion counts were exported from Compound Discoverer and
508 normalized to biomass (either total DNA or total protein). DNA was quantified from cell
509 pellets after metabolite extraction using IBI Scientific genomic DNA kit for cultured cells as
510 previously described for metabolite normalization following kit instructions (49). Total
511 protein was quantified using the Pierce BCA Protein Assay Kit from separately cultured and
512 harvested samples in parallel with metabolomics experiments.

513 *Quantification of Total Ketone Bodies*

514 Acetoacetate (AcAc) and β-hydroxybutyrate (BOHB) were formally quantified using UHPLC-
515 MS/MS as described previously (50, 51). Briefly, [U-$^{13}C_4$]AcAc and [3,4,4,4-D4]βOHB internal
516 standards were spiked into ice cold MeOH:ACN (1:1), then ketones were extracted,
517 separated via reverse-phase UHPLC, and detected via parallel reaction monitoring (PRM) on
518 a QExactive Plus hybrid quadrupole-orbitrap mass spectrometer.

519 *Bulk RNA sequencing and analysis*

520 For the 2D platform, cells were collected from the plates using 0.25% Trypsin-EDTA. For the
521 3D platform, microtissues were collected from the wells and dissociated by incubating at
522 37°C with 0.1mg/mL Collagenase Type IV in HBSS (+CaCl2, +MgCl2) for 30 minutes, then
523 manually disrupted to form a single cell suspension. For both platforms, 8 wells were
524 combined to form replicates, n=3 per group. The single cell suspensions were incubated with
525 MicroBeads against human CD326 (EpCAM) and antibody against CD16/CD32 to block

526 nonspecific binding, then isolated across Miltenyi LS magnetic separation columns. RNA
527 was isolated from the sorted SW480 cells using a Qiagen RNeasy Mini Kit.

528 **Bulk RNA-seq Analysis**. RNA-seq analysis was performed at the Minnesota
529 Supercomputing Institute at the University of Minnesota. Briefly, Fastq files were first
530 processed with the CHURP pipeline (version 0.2.3) (52) to perform adaptor trimming using
531 trimmomatic (version 0.33) (53); reads were then mapped to Homo sapiens GRCh38
532 genome using HiSat2 (version 2.1.0) (54). Subreads count was generated using the Subreads
533 featureCounts tool (version 1.6.2) (55) using the Homo_sapiens.GRCh38.100.gtf annotation.
534 Count data were filtered by removing genes that were less than 300 nt in length and including
535 only genes that had a cpm (counts per million) value greater than 1 cpm in at least two
536 sample replicates. The quasi-likelihood test was used to evaluate differential expression
537 (DE) with edgeR (version 3.38.1) (56, 57). The Benjamini-Hochberg method was used to
538 adjust p-values for multiple hypothesis testing and an adjusted p-value ≤ 0.05, with a log2
539 fold change > 0 was used as a DE significance threshold. For gene ontology (GO pathway and
540 GSEA analysis, the R package clusterProfiler (version 4.4.4) (58, 59) was used. Normalized
541 Enrichment Score (NES) indicates the distribution of genes across a ranked list and
542 normalizes the correlation between gene sets and datasets to gene set size, allowing for
543 comparison. For GSEA analysis specifically, Hallmark and 18 selected C2 pathways were
544 combined and used for testing (see full GSEA pathway results and selected C2 pathways in
545 **Supplemental Table 1, 2**). Analysis of GSEA C6 oncogenic pathways, read counts were
546 converted to normalized counts using the DESeq2 (version 1.42.0) R package and were
547 further filtered to get rid of genes with zero expression across all samples. GSEA was then

548 performed using the standalone software (version 4.3.2) developed by the Broad Institute,
549 and statistical significance was assessed via gene set permutation testing (1000
550 permutations) (60, 61). GEO accession number GSE282081.

551 *Statistics and Multi-omic Analysis*

552 Descriptive data are expressed as mean and standard error (SEM) for continuous measures.
553 Comparison of metabolite abundance were made between HJ and SJH or SJ and SJH by
554 unpaired t-test and corrected for multiple comparisons by Benjamini-Hochberg using
555 GraphPrism v10.2.3. Multi-omic integration of bulk transcriptomic and metabolomics
556 datasets were performed in R v4.2.3 using rcorr() from the Hmisc package and the igraph
557 package for visualization of correlations. Given the small dataset, only highly significant
558 correlations (p-value of Pearson correlation coefficient < 0.001) were included in
559 downstream pathway and gene ontology analysis. Genes that correlated strongly with
560 metabolites of interest were included as a set of gene IDs and fold changes in an
561 ExpressAnalyst query for functional analysis (62).

562 Discriminant ITUM was performed using a curated dataset of positively identified
563 metabolites by commercial standard and / or MS/MS match in mzCloud. Selected
564 metabolites showed significant total enrichment in the SJH group after correction for natural
565 abundance of ^{13}C (1.11% of all carbon in nature), performed within the Compound
566 Discoverer "stable isotope labeling" node based on predicted chemical formula. All
567 isotopologues with enrichment were included for a given metabolite as individual variables,
568 *i.e.* S_M0, S_M1, S_M2, S_M3 included as four unique variables representing serine
569 enrichment. Data presented in 0-100 range and represents percentage of the total

570 metabolite pool detected by LC-MS in full scan (MS1). Total pools are calculated by sum of
571 ion counts for each possible isotopologue (*i.e.* total ion counts of serine = S_M0 + S_M1 +
572 S_M2 + S_M3; % Enrichment of S_M3 = ion counts of S_M3 / total ion counts of serine * 100).
573 The resulting multivariate dataset was used for Principal Components Analysis (PCA) to
574 identify co-enriched isotopologues that discriminate SJH co-cultures from SJ or HJ controls.
575 PCA was performed in GraphPrism v10.2.3. Data was standardized prior to PCA. A
576 correlation network was graphed from the top contributing isotopologues distinguishing SJH
577 from SJ controls using the igraph package in the R environment for qualitative pathway
578 analysis of glucose utilization in mixed cell populations. Joint pathway analysis of 3D
579 microtissue transcriptomics and metabolomics datasets performed in MetaboAnalyst 4.0
580 (63).
581

582 Acknowledgements: We are grateful to Alisha Seay for technical support. This study was
583 funded by the University of Minnesota, Medical School Dean's Academic Investment
584 Research Program (AIRP). Additional funding: T32DK007203 (ABN); R01CA215052 (KLS);
585 HL166142 (EDQ).

References

1. Siegel RL, Giaquinto AN, and Jemal A. Cancer statistics, 2024. *CA: A Cancer Journal for Clinicians*. 2024;74(1):12-49.
2. Horn SR, Stoltzfus KC, Lehrer EJ, Dawson LA, Tchelebi L, Gusani NJ, et al. Epidemiology of liver metastases. *Cancer Epidemiology*. 2020;67:101760.
3. Hanahan D, and Weinberg Robert A. Hallmarks of Cancer: The Next Generation. *Cell*. 2011;144(5):646-74.
4. Pavlova Natalya N, and Thompson Craig B. The Emerging Hallmarks of Cancer Metabolism. *Cell Metabolism*. 2016;23(1):27-47.
5. Lyssiotis CA, and Kimmelman AC. Metabolic Interactions in the Tumor Microenvironment. *Trends in Cell Biology*. 2017;27(11):863-75.
6. Sullivan MR, Danai LV, Lewis CA, Chan SH, Gui DY, Kunchok T, et al. Quantification of microenvironmental metabolites in murine cancers reveals determinants of tumor nutrient availability. *eLife*. 2019;8:e44235.
7. Lin J, Rao D, Zhang M, and Gao Q. Metabolic reprogramming in the tumor microenvironment of liver cancer. *Journal of Hematology & Oncology*. 2024;17(1):6.
8. Huang Q, Tan Y, Yin P, Ye G, Gao P, Lu X, et al. Metabolic Characterization of Hepatocellular Carcinoma Using Nontargeted Tissue Metabolomics. *Cancer Research*. 2013;73(16):4992-5002.
9. Nwosu ZC, Megger DA, Hammad S, Sitek B, Roessler S, Ebert MP, et al. Identification of the Consistently Altered Metabolic Targets in Human Hepatocellular Carcinoma. *Cellular and Molecular Gastroenterology and Hepatology*. 2017;4(2):303-23.e1.
10. Dupuy F, Tabariès S, Andrzejewski S, Dong Z, Blagih J, Annis Matthew G, et al. PDK1-Dependent Metabolic Reprogramming Dictates Metastatic Potential in Breast Cancer. *Cell Metabolism*. 2015;22(4):577-89.
11. Bu P, Chen K-Y, Xiang K, Johnson C, Crown SB, Rakhilin N, et al. Aldolase B-Mediated Fructose Metabolism Drives Metabolic Reprogramming of Colon Cancer Liver Metastasis. *Cell Metabolism*. 2018;27(6):1249-62.e4.
12. Loo Jia M, Scherl A, Nguyen A, Man Fung Y, Weinberg E, Zeng Z, et al. Extracellular Metabolic Energetics Can Promote Cancer Progression. *Cell*. 2015;160(3):393-406.
13. Clish CB. Metabolomics: an emerging but powerful tool for precision medicine. *Cold Spring Harb Mol Case Stud*. 2015;1(1):a000588.
14. Patti GJ, Yanes O, and Siuzdak G. Innovation: Metabolomics: the apogee of the omics trilogy. *Nat Rev Mol Cell Biol*. 2012;13(4):263-9.
15. Nelson AB, Chow LS, Stagg DB, Gillingham JR, Evans MD, Pan M, et al. Acute aerobic exercise reveals FAHFAs distinguish the metabolomes of overweight and normal weight runners. *JCI Insight*. 2022.
16. Jang C, Chen L, and Rabinowitz JD. Metabolomics and Isotope Tracing. *Cell*. 2018;173(4):822-37.
17. Puchalska P, Martin SE, Huang X, Lengfeld JE, Daniel B, Graham MJ, et al. Hepatocyte-Macrophage Acetoacetate Shuttle Protects against Tissue Fibrosis. *Cell Metab*. 2019;29(2):383-98 e7.

18. Stagg DB, Gillingham JR, Nelson AB, Lengfeld JE, d'Avignon DA, Puchalska P, et al. Diminished ketone interconversion, hepatic TCA cycle flux, and glucose production in D-β-hydroxybutyrate dehydrogenase hepatocyte-deficient mice. *Molecular Metabolism*. 2021;53:101269.
19. Puchalska P, Huang X, Martin SE, Han X, Patti GJ, and Crawford PA. Isotope Tracing Untargeted Metabolomics Reveals Macrophage Polarization-State-Specific Metabolic Coordination across Intracellular Compartments. *iScience*. 2018;9:298-313.
20. Buescher JM, Antoniewicz MR, Boros LG, Burgess SC, Brunengraber H, Clish CB, et al. A roadmap for interpreting 13C metabolite labeling patterns from cells. *Current Opinion in Biotechnology*. 2015;34:189-201.
21. Muir A, Danai LV, and Vander Heiden MG. Microenvironmental regulation of cancer cell metabolism: implications for experimental design and translational studies. *Disease Models & Mechanisms*. 2018;11(8):dmm035758.
22. Xiang C, Du Y, Meng G, Soon Yi L, Sun S, Song N, et al. Long-term functional maintenance of primary human hepatocytes in vitro. *Science*. 2019;364(6438):399-402.
23. Sun P, Zhang G, Su X, Jin C, Yu B, Yu X, et al. *Cell Reports*. 2019;29(10):3212-22.e4.
24. Kukla DA, Crampton AL, Wood DK, and Khetani SR. Microscale Collagen and Fibroblast Interactions Enhance Primary Human Hepatocyte Functions in Three-Dimensional Models. *Gene expression*. 2020;20(1):1-18.
25. DeBerardinis RJ, and Chandel NS. We need to talk about the Warburg effect. *Nature Metabolism*. 2020;2(2):127-9.
26. Warburg O. The metabolism of carcinoma cells. *The Journal of Cancer Research*. 1925;9(1):148-63.
27. Ma EH, Verway MJ, Johnson RM, Roy DG, Steadman M, Hayes S, et al. Metabolic Profiling Using Stable Isotope Tracing Reveals Distinct Patterns of Glucose Utilization by Physiologically Activated CD8⁺ T Cells. *Immunity*. 2019;51(5):856-70.e5.
28. Liberti MV, and Locasale JW. The Warburg Effect: How Does it Benefit Cancer Cells? *Trends Biochem Sci*. 2016;41(3):211-8.
29. Deng Y, Wang ZV, Gordillo R, An Y, Zhang C, Liang Q, et al. An adipo-biliary-uridine axis that regulates energy homeostasis. *Science*. 2017;355(6330).
30. Puchalska P, and Crawford PA. In: Stover PJ, and Balling R eds. *Annual Review of Nutrition, Vol 41, 2021*. 2021:49-77.
31. Camarero N, Mascaró C, Mayordomo C, Vilardell F, Haro D, and Marrero PF. Ketogenic HMGCS2 Is a c-Myc target gene expressed in differentiated cells of human colonic epithelium and down-regulated in colon cancer. *Mol Cancer Res*. 2006;4(9):645-53.
32. Wang YH, Liu CL, Chiu WC, Twu YC, and Liao YJ. HMGCS2 Mediates Ketone Production and Regulates the Proliferation and Metastasis of Hepatocellular Carcinoma. *Cancers (Basel)*. 2019;11(12).
33. Zou K, Hu Y, Li M, Wang H, Zhang Y, Huang L, et al. Potential Role of HMGCS2 in Tumor Angiogenesis in Colorectal Cancer and Its Potential Use as a Diagnostic Marker. *Can J Gastroenterol Hepatol*. 2019;2019:8348967.

673 34. Zhang J, Jia PP, Liu QL, Cong MH, Gao Y, Shi HP, et al. Low ketolytic enzyme levels in
674 tumors predict ketogenic diet responses in cancer cell lines in vitro and in vivo. *J Lipid*
675 *Res*. 2018;59(4):625-34.
676 35. Shukla SK, Gebregiworgis T, Purohit V, Chaika NV, Gunda V, Radhakrishnan P, et al.
677 Metabolic reprogramming induced by ketone bodies diminishes pancreatic cancer
678 cachexia. *Cancer Metab*. 2014;2:18.
679 36. Sperry J, Condro MC, Guo L, Braas D, Vanderveer-Harris N, Kim KKO, et al.
680 Glioblastoma Utilizes Fatty Acids and Ketone Bodies for Growth Allowing Progression
681 during Ketogenic Diet Therapy. *iScience*. 2020;23(9):101453.
682 37. Xia S, Lin R, Jin L, Zhao L, Kang HB, Pan Y, et al. Prevention of Dietary-Fat-Fueled
683 Ketogenesis Attenuates BRAF V600E Tumor Growth. *Cell Metab*. 2017;25(2):358-73.
684 38. Lima WG, Martins-Santos ME, and Chaves VE. Uric acid as a modulator of glucose
685 and lipid metabolism. *Biochimie*. 2015;116:17-23.
686 39. Yiu A, Van Hemelrijck M, Garmo H, Holmberg L, Malmström H, Lambe M, et al.
687 Circulating uric acid levels and subsequent development of cancer in 493,281
688 individuals: findings from the AMORIS Study. *Oncotarget*. 2017;8(26):42332-42.
689 40. Fini MA, Elias A, Johnson RJ, and Wright RM. Contribution of uric acid to cancer risk,
690 recurrence, and mortality. *Clin Transl Med*. 2012;1(1):16.
691 41. Nwosu ZC, Ward MH, Sajjakulnukit P, Poudel P, Ragulan C, Kasperek S, et al. Uridine-
692 derived ribose fuels glucose-restricted pancreatic cancer. *Nature*.
693 2023;618(7963):151-8.
694 42. Skinner OS, Blanco-Fernández J, Goodman RP, Kawakami A, Shen H, Kemény LV, et
695 al. Salvage of ribose from uridine or RNA supports glycolysis in nutrient-limited
696 conditions. *Nature Metabolism*. 2023;5(5):765-76.
697 43. Dong Y, Tu R, Liu H, and Qing G. Regulation of cancer cell metabolism: oncogenic
698 MYC in the driver's seat. *Signal Transduction and Targeted Therapy*. 2020;5(1):124.
699 44. Chen C-Y, Chen J, He L, and Stiles BL. PTEN: Tumor Suppressor and Metabolic
700 Regulator. *Frontiers in Endocrinology*. 2018;9.
701 45. Zhang X, Zhao H, Li Y, Xia D, Yang L, Ma Y, et al. The role of YAP/TAZ activity in cancer
702 metabolic reprogramming. *Molecular Cancer*. 2018;17(1):134.
703 46. Puchalska P, and Crawford PA. Application of Stable Isotope Labels for Metabolomics
704 in Studies in Fatty Liver Disease. *Methods Mol Biol*. 2019;1996:259-72.
705 47. Ivanisevic J, Zhu Z-J, Plate L, Tautenhahn R, Chen S, O'Brien PJ, et al. Toward 'Omic
706 Scale Metabolite Profiling: A Dual Separation–Mass Spectrometry Approach for
707 Coverage of Lipid and Central Carbon Metabolism. *Analytical Chemistry*.
708 2013;85(14):6876-84.
709 48. Koelmel JP, Kroeger NM, Gill EL, Ulmer CZ, Bowden JA, Patterson RE, et al. Expanding
710 Lipidome Coverage Using LC-MS/MS Data-Dependent Acquisition with Automated
711 Exclusion List Generation. *Journal of the American Society for Mass Spectrometry*.
712 2017;28(5):908-17.
713 49. Silva LP, Lorenzi PL, Purwaha P, Yong V, Hawke DH, and Weinstein JN. Measurement
714 of DNA Concentration as a Normalization Strategy for Metabolomic Data from
715 Adherent Cell Lines. *Analytical Chemistry*. 2013;85(20):9536-42.

50. Puchalska P, Nelson AB, Stagg DB, and Crawford PA. Determination of ketone bodies in biological samples via rapid UPLC-MS/MS. *Talanta*. 2021;225:122048.
51. Queathem ED, Nelson AB, and Puchalska P. In: Giera M, and Sánchez-López E eds. *Clinical Metabolomics: Methods and Protocols*. New York, NY: Springer US; 2025:117-31.
52. Baller J, Kono T, Herman A, and Zhang Y. *Practice and Experience in Advanced Research Computing 2019: Rise of the Machines (learning)*. Chicago, IL, USA: Association for Computing Machinery; 2019:Article 96.
53. Bolger AM, Lohse M, and Usadel B. Trimmomatic: a flexible trimmer for Illumina sequence data. *Bioinformatics*. 2014;30(15):2114-20.
54. Kim D, Langmead B, and Salzberg SL. HISAT: a fast spliced aligner with low memory requirements. *Nature Methods*. 2015;12(4):357-60.
55. Liao Y, Smyth GK, and Shi W. The Subread aligner: fast, accurate and scalable read mapping by seed-and-vote. *Nucleic Acids Research*. 2013;41(10):e108-e.
56. McCarthy DJ, Chen Y, and Smyth GK. Differential expression analysis of multifactor RNA-Seq experiments with respect to biological variation. *Nucleic Acids Res*. 2012;40(10):4288-97.
57. Robinson MD, McCarthy DJ, and Smyth GK. edgeR: a Bioconductor package for differential expression analysis of digital gene expression data. *Bioinformatics*. 2009;26(1):139-40.
58. The Gene Ontology Consortium. The Gene Ontology Resource: 20 years and still GOing strong. *Nucleic Acids Research*. 2018;47(D1):D330-D8.
59. Yu G, Wang LG, Han Y, and He QY. clusterProfiler: an R package for comparing biological themes among gene clusters. *Omics*. 2012;16(5):284-7.
60. Love MI, Huber W, and Anders S. Moderated estimation of fold change and dispersion for RNA-seq data with DESeq2. *Genome Biology*. 2014;15(12):550.
61. Subramanian A, Tamayo P, Mootha VK, Mukherjee S, Ebert BL, Gillette MA, et al. Gene set enrichment analysis: a knowledge-based approach for interpreting genome-wide expression profiles. *Proc Natl Acad Sci U S A*. 2005;102(43):15545-50.
62. Ewald J, Zhou G, Lu Y, and Xia J. Using ExpressAnalyst for Comprehensive Gene Expression Analysis in Model and Non-Model Organisms. *Current Protocols*. 2023;3(11):e922.
63. Chong J, and Xia J. Using MetaboAnalyst 4.0 for Metabolomics Data Analysis, Interpretation, and Integration with Other Omics Data. *Methods Mol Biol*. 2020;2104:337-60.

753 **Tables**

754 **Table 1.** Differential abundance of select metabolites in SJH co-cultures relative to HJ or SJ
755 controls. FC: fold change; ctrl: control.

Putative metabolite	Log_2 (FC: SJH / ctrl)	Adjusted p-value	Direction; Relative to [HJ] or [SJ]
S-Adenosylhomocysteine	1.87	0.0004	↑; HJ
Pyruvate	-1.05	0.0001	↓; HJ
Acetyl-CoA	-1.98	0.002	↓; HJ
Propionyl-CoA	-1.89	0.012	↓; HJ
Propionyl-CoA	5.01	0.0004	↑; SJ
Glutamyl-glycine	2.47	0.00007	↑; SJ
Acetyl-CoA	1.63	0.016	↑; SJ
Pyruvate	-3.60	0.0006	↓; SJ
Lactate	-2.78	0.0012	↓; SJ
NAD^+	-1.85	0.012	↓; SJ
ATP	-1.09	0.03	↓; SJ

756

757

758 **Table 2.** Differential abundance of select metabolites in SJH co-cultures relative to 1T1
759 dilution. Abbreviations: FC: fold change

Putative metabolite	Log_2 (FC: SJH / HJ)	Adjusted p-value	Direction relative to 1T1
Glutamyl-glycine	2.59	0.0018	↑
Uracil	2.24	0.0044	↑
Uridine diphosphate	1.42	0.021	↑
Aspartate	1.17	0.0018	↑
Malate	1.03	0.0029	↑
Lactate	-1.08	0.013	↓

760

761

762

Table 3. Fold change in extracellular and intracellular metabolite abundance after 24-hour incubation relative to starting media (t0). Adjusted p-value by t-test comparing T24 abundance to T0 abundance with BH correction for multiple testing. Abbreviations: FC: fold change; E: Extracellular; I: Intracellular; NC: no change.

	Log_2(FC: T24 / T0) [adj. p-value]			
Putative metabolite (E/I)	**HJ**	**SJH**	**SJ**	**Direction relative to T0**
Hypoxanthine (E)	-1.36 [<0.0001]	-2.62 [<0.0001]	-4.73 [<0.00001]	↓; ↓; ↓
Uric Acid (E)	-3.97 [<0.001]	-4.20 [<0.001]	3.17 [<0.001]	↓; ↓; ↑
Inosine (I)	1.00 [0.002]	1.27 [0.003]	-0.42 [0.27]	↑; ↑; NC
Uridine (E)	2.36 [<0.0001]	1.94 [<0.001]	-0.50 [0.15]	↑; ↑; NC
Orotic Acid (E)	4.27 [<0.00001]	4.19 [<0.001]	0.40 [<0.001]	↑; ↑; ↑
Aspartate (I)	0.04 [0.87]	0.55 [0.02]	-0.11 [0.49]	NC; ↑; NC
Carbamoyl aspartate (I)	-0.16 [0.19]	5.47 [0.036]	-0.17 [>0.99]	NC; ↑; NC
UDP (I)	0.32 [0.62]	1.44 [0.017]	0.51 [0.33]	NC; ↑; NC
Uridine (I)	1.13 [0.10]	3.23 [0.005]	-0.25 [0.33]	NC; ↑; NC
Orotic Acid (I)	0.09 [0.62]	3.48 [0.029]	-0.38 [0.37]	NC; ↑; NC

769 **Figure Legends**

770 **Figure 1. Multiomic study of co-cultures of primary hepatocytes and SW480s.** (A)
771 Scheme of 2D co-culture system and timeline for cell collection. (B) -Omic coverage of co-
772 cultured groups.

773

774 **Figure 2. Fuel utilization in 2-dimensional co-cultures.** (A) Glucose consumption and
775 lactate production in moles per ng total DNA per day. (B) Lactate / glucose ratio of media
776 concentration after 24h. (C) Concentration of acetoacetate (AcAc), β-hydroxybutyrate
777 (βOHB) and total ketone bodies (TKB) in mmol/g DNA measured in media after 24h
778 incubation. (D) Relative abundance of glutamine in total ion counts after normalization to
779 total ng DNA. Volcano plot showing upregulated and downregulated metabolites in SJH
780 compared to: (E) HJ control cultures and (F) SJ control cultures; positive $\log_2$FC = up in SJH.
781 Significance tested using unpaired t-test, comparison HJ vs SJH or SJ vs SJH, and corrected
782 for multiple comparisons using Benjamini-Hochberg method. *: p adj. < 0.05, **: p adj. <
783 0.01, ***: p adj. < 0.001, ****: p adj. < 0.0001. Abbreviations: HJ: Hepatocyte+3T3-J2 co-
784 culture; SJH: SW480+3T3-J2+Hepatocyte co-culture; SJ: SW480+3T3-J2 co-culture.

785

786 **Figure 3. Analytical dilution of co-culture controls reveals metabolic adaptation in SJH**
787 **co-cultures.** (A) Schematic of analytical dilution of HJ and SJ controls to form a 1-to-1 ratio
788 (1T1) after metabolite extraction. (B) Volcano plot upregulated and downregulated
789 metabolites in SJH compared to 1T1 ion counts; positive $\log_2$FC = up in SJH.

790

791 **Figure 4. Metabolic interactions of biosynthetic pathways in SJH co-cultures.** Fold
792 change of metabolite abundance after 24h co-culture relative to time point 0 in: (A) media
793 abundance of purine metabolism products, hypoxanthine and uric acid, (B) intracellular
794 inosine pools, (D) media abundance of pyrimidine biosynthesis intermediates, uridine and
795 orotic acid, and (E) intracellular pyrimidine intermediates and substrates, aspartate,
796 carbamoyl aspartate, orotic acid, UDP, and uridine. (C) ^{13}C-enrichment of intracellular
797 inosine pools from 22 mM [U-$^{13}C_6$]glucose in 3D microtissue organoids. Statistical
798 comparison by unpaired t-test; letters indicate significance in comparison to HJ controls
799 ("a") or SJ controls ("b").

800

801 **Figure 5. Discriminant ITUM analysis of SJH co-cultures.** (A) Biplot of first two principal
802 components (PC1, PC2) of PCA of HJ, SJH, and SJ co-cultures by ^{13}C-glucose-enriched

803 isotopologues. Black filled circles represent samples. Spheres show co-culture groups. Blue
804 directed vectors show isotopologue loadings for PC1 and PC2. (B) Hierarchical clustering of
805 ITUM SJH vs SJ Pearson correlation matrix. White triangle with "1" label indicates control
806 cluster of isotopologues; Yellow shapes with "2" and "3" label corresponds to cluster of
807 isotopologues from region of strongly co-enriched isotopologues in response to co-culture;
808 Black shapes with "4" label corresponds to cluster of isotopologues with weak co-
809 enrichment in response to co-culture. Red arrow, U_M6 positive correlation with unenriched
810 M+0 isotopologues in Region 1; Blue arrow, U_M6 negative correlation with multiple
811 isotopologues including GSH_M3 in Region 2; Yellow arrow, GSH_M4 positive correlation
812 with metabolic precursor E_M4 in Region 3. Abbreviations: M#: isotopologue representing
813 number of heavy carbons present in the molecule (*i.e.,* M1 indicates presence of 1 heavy 13-
814 carbon), aKG: alpha-ketoglutarate, S: serine, M: Malate, L: lactate, C: citrate, ATP: adenosine
815 triphosphate, U: uridine diphosphate N-Acetylglucosamine, G: glycine, D: Asparate, E:
816 Glutamate, GSH: glutathione, Sc: Succinate, GPI: glycerophosphoinositol.

817

818 **Figure 6. Transcriptional profiling of tumor cells in 3D microtissues identifies**
819 **alterations in metabolic pathways upon exposure to hepatocytes**. (A) 3D microtissue
820 organoid scheme. (B) Volcano plot showing significantly upregulated and downregulated
821 genes in samples from SJH cultures compared with SJ cultures. Positive logFC indicates up
822 in SJH cultures. (C) Gene ontology analysis using DEG as input. (D) GSEA Hallmark analysis
823 of SJ compared with SJH. A positive NES score indicates gene profiles that are enriched in
824 tumor cells from the SJH condition compared with the SJ condition. All shown pathways
825 adjusted FDR < 0.05. (E) Expression patterns of core enriched genes associated with Myc
826 pathway and two metabolic pathways, oxidative phosphorylation and glutathione
827 metabolism, that are positively enriched in the SJH condition and heat maps. (F) GSEA
828 Oncogenic analysis of SJ compared with SJH. A negative NES score indicates gene profiles
829 that are enriched in tumor cells from the SJ condition compared with the SJH condition. All
830 shown pathways adjusted FDR < 0.05.

831 **Figure 7. Multiomic pathway analysis of metabolic adaptation to hepatocytes.** (A)
832 Correlation network of differentially expressed genes (DEGs) and metabolites in SJH co-
833 cultures compared to SJ control cultures. Gene names filtered from full bulk RNA-
834 sequencing DEGs for significance of correlation to metabolites of interest ($p < 0.001$). Red
835 lines indicate strong positive associations and blue represent strong negative associations
836 ($R > |0.98|$). (B) Hierarchical clustering of Pearson correlation matrix of transcripts highly
837 correlated with glutamyl-glycine (Glu-Gly). (C) Gene counts with functional group
838 membership of 98 transcripts found to correlate strongly with glutamyl-glycine (Glu-Gly)

Supplemental Figure 1. Metabolite abundance in 2D co-cultures. Ion counts after normalization to total ng DNA of: (A) pyruvate, (B) Acetyl-CoA, (C) Propionyl-CoA, (D) Lactate, (E) NAD^+, (F) NADH, and (H) AMP, ADP, ATP nucleotides. (G) Ratio of NAD^+ to NADH ion counts. (I) Calculated energy charge of each co-culture group based on ion counts of AMP, ADP, and ATP. Significance tested using unpaired t-test, comparison HJ vs SJH or SJ vs SJH, and corrected for multiple comparisons using Benjamini-Hochberg method. *: p adj. < 0.05, **: p adj. < 0.01, ***: p adj. < 0.001, ****: p adj. < 0.0001.

Supplemental Figure 2. Lactate abundance in co-culture and 1T1 dilution. Bar graph of total ion counts after normalization to DNA compared to analytical dilution (1T1). Significance tested using unpaired t-test, comparison HJ vs SJH or SJ vs SJH, and 1T1 vs SJH; corrected for multiple comparisons using Benjamini-Hochberg method. *: p adj. < 0.05, **: p adj. < 0.01

Supplemental Figure 3. Percent change in media purines. Percent difference in media after 24h incubation with co-cultured cells where time point 0 represents starting media abundance prior to cell exposure. Dotted lines represent accumulation of hypoxanthine (Hpx) and uric acid (UA) after 24h at 37°C in media in absence of cells. Statistical comparison by unpaired t-test; letters indicate significance in comparison to HJ controls ("a") or SJ controls ("b").

Supplemental Figure 4. Correlation matrix of SJH vs HJ ITUM in 2D co-cultures. Correlation matrix assessing co-enriched isotopologues in response to presence of hepatocytes (SJ, SJH cultures). Red gradient represents positive associations while blue represents negative associations. Correlations measuring by Pearson correlation method.

Supplemental Figure 5. Distribution of ^{13}C enrichment. Percent enrichment of total pools of (A) Uridine diphosphate N-acetyglucosamine and (B) glutathione after 24h incubation with [U-$^{13}C_6$]glucose at 37°C. *: p adj. < 0.05

Supplemental Figure 6. Multiomic pathway analysis. (A) Gene counts with functional group membership of 151 genes found to correlate strongly with glutamyl-glycine (Glu-Gly), orotic acid, lactate, uridine monophosphate, and malate. (B) Functional network of shared genes in represented transcriptional profile with strong metabolite-gene associations; analysis performed using ExpressAnalyst. (C) Scatter plot of joint pathway analysis from MetaboAnalyst v4.0 using DEGs and full static metabolomics dataset based on associated fold changes. X and y axes show enrichment score in genes and metabolite peaks, respectively.

Figure 1

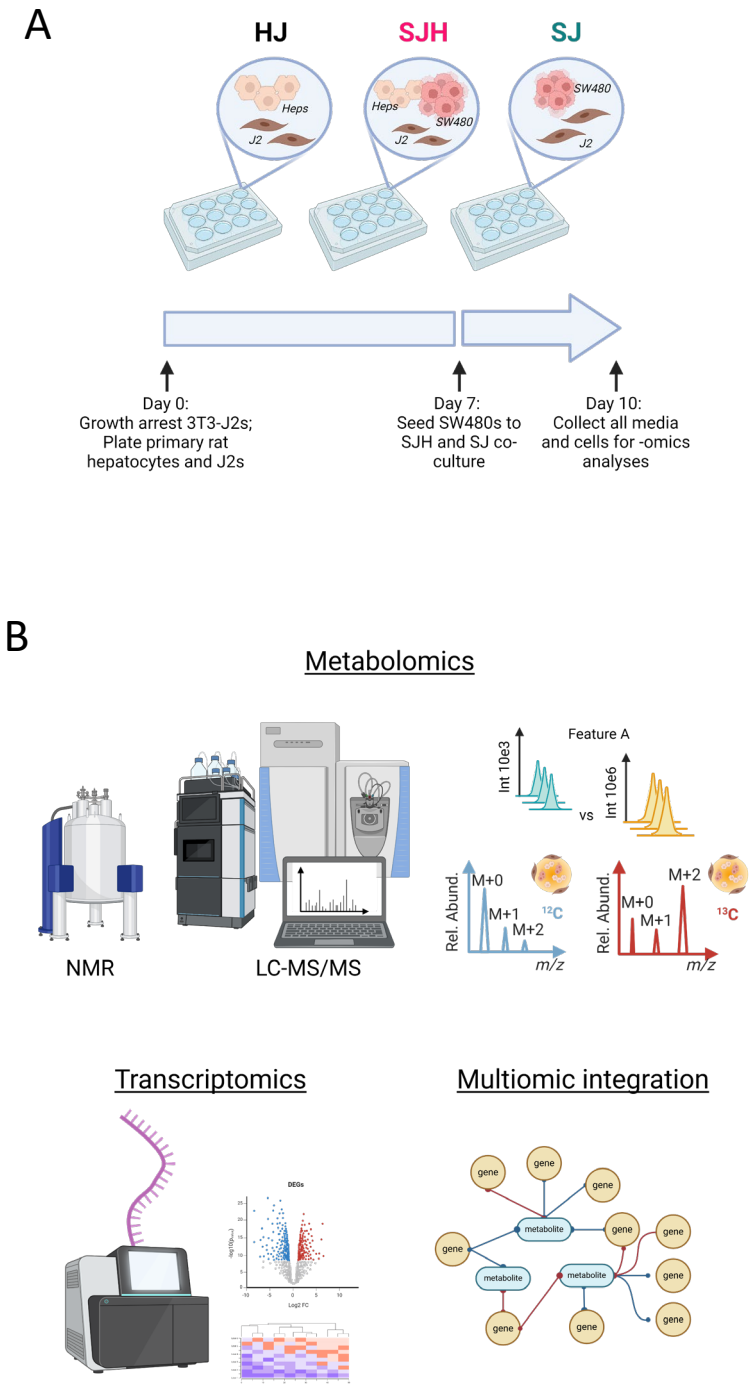
A
HJ
SJH
SJ
Heps
J2
Heps
SW480
J2
SW480
J2
Day 0:
Growth arrest 3T3-J2s;
Plate primary rat
hepatocytes and J2s
Day 7:
Seed SW480s to
SJH and SJ co-
culture
Day 10:
Collect all media
and cells for -omics
analyses
B
Metabolomics
NMR
LC-MS/MS
Feature A
Int 10e3
vs
Int 10e6
Rel. Abund.
M+0
M+1
M+2
12C
m/z
Rel. Abund.
M+0
M+1
M+2
13C
m/z
Transcriptomics
DEGs
Multiomic integration
gene
metabolite

Figure 2

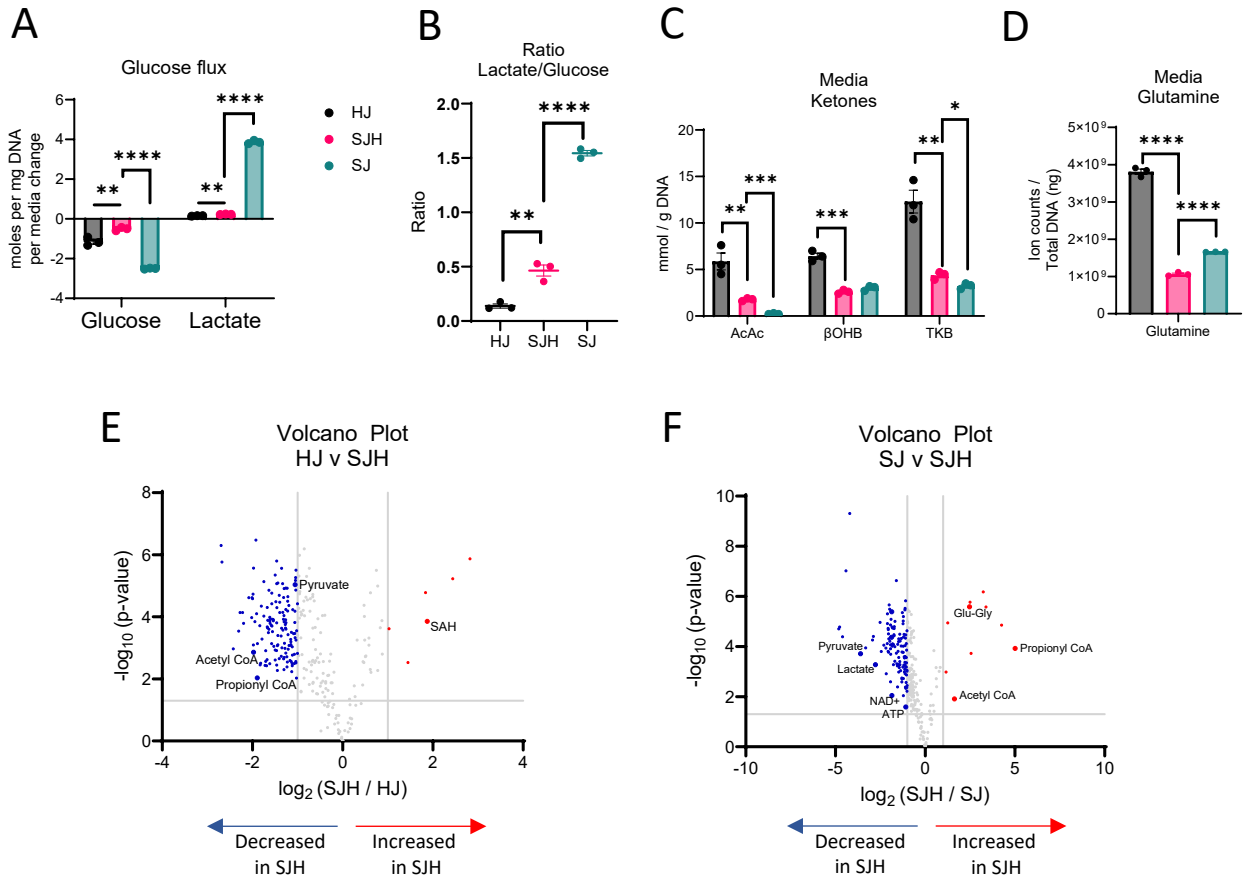
A
Glucose flux
moles per mg DNA per media change
Glucose
Lactate
HJ
SJH
SJ
B
Ratio Lactate/Glucose
Ratio
HJ
SJH
SJ
C
Media Ketones
mmol / g DNA
AcAc
βOHB
TKB
D
Media Glutamine
Ion counts / Total DNA (ng)
Glutamine
E
Volcano Plot HJ v SJH
-log10 (p-value)
log2 (SJH / HJ)
Pyruvate
SAH
Acetyl CoA
Propionyl CoA
Decreased in SJH
Increased in SJH
F
Volcano Plot SJ v SJH
-log10 (p-value)
log2 (SJH / SJ)
Glu-Gly
Propionyl CoA
Pyruvate
Lactate
NAD+
ATP
Acetyl CoA
Decreased in SJH
Increased in SJH

Figure 3

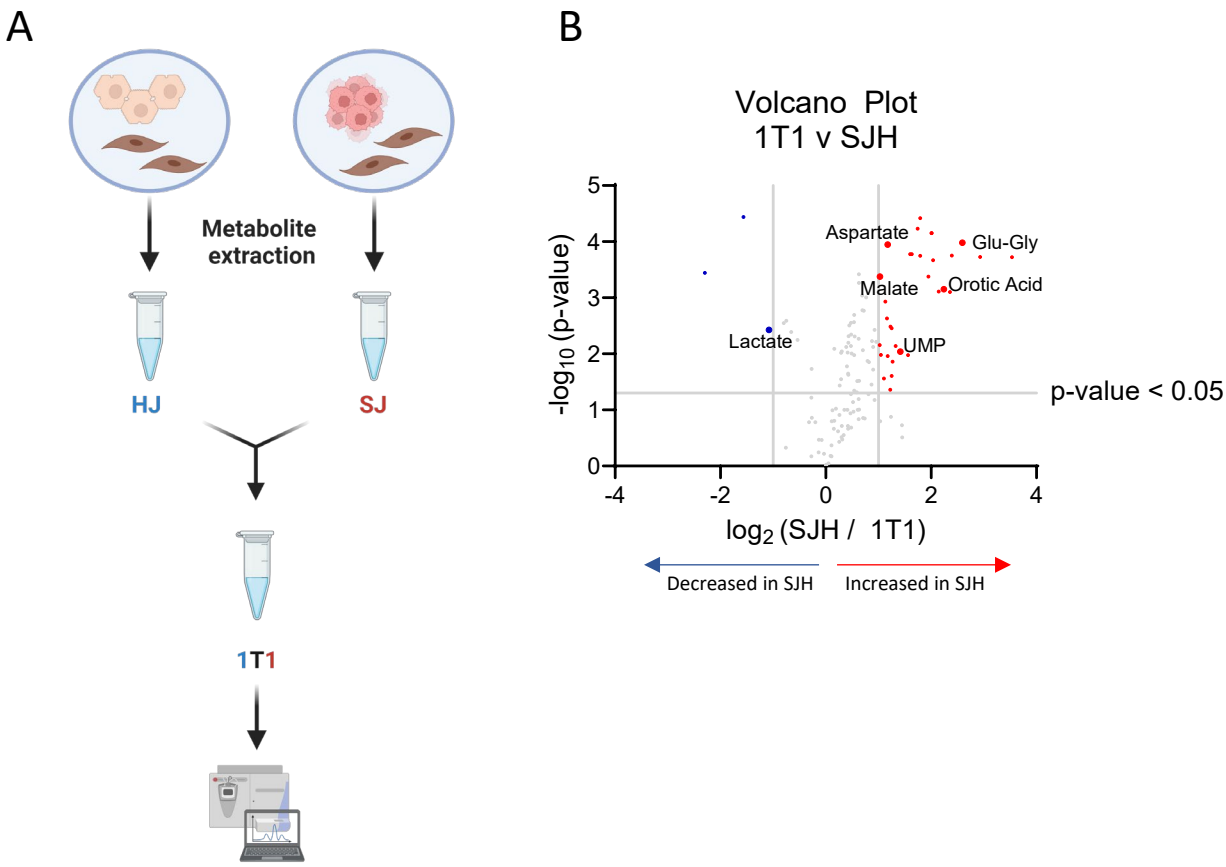
A
Metabolite extraction
HJ
SJ
1T1
B
Volcano Plot
1T1 v SJH
-log10 (p-value)
log2 (SJH / 1T1)
Aspartate
Glu-Gly
Malate
Orotic Acid
Lactate
UMP
p-value < 0.05
Decreased in SJH
Increased in SJH

Figure 4

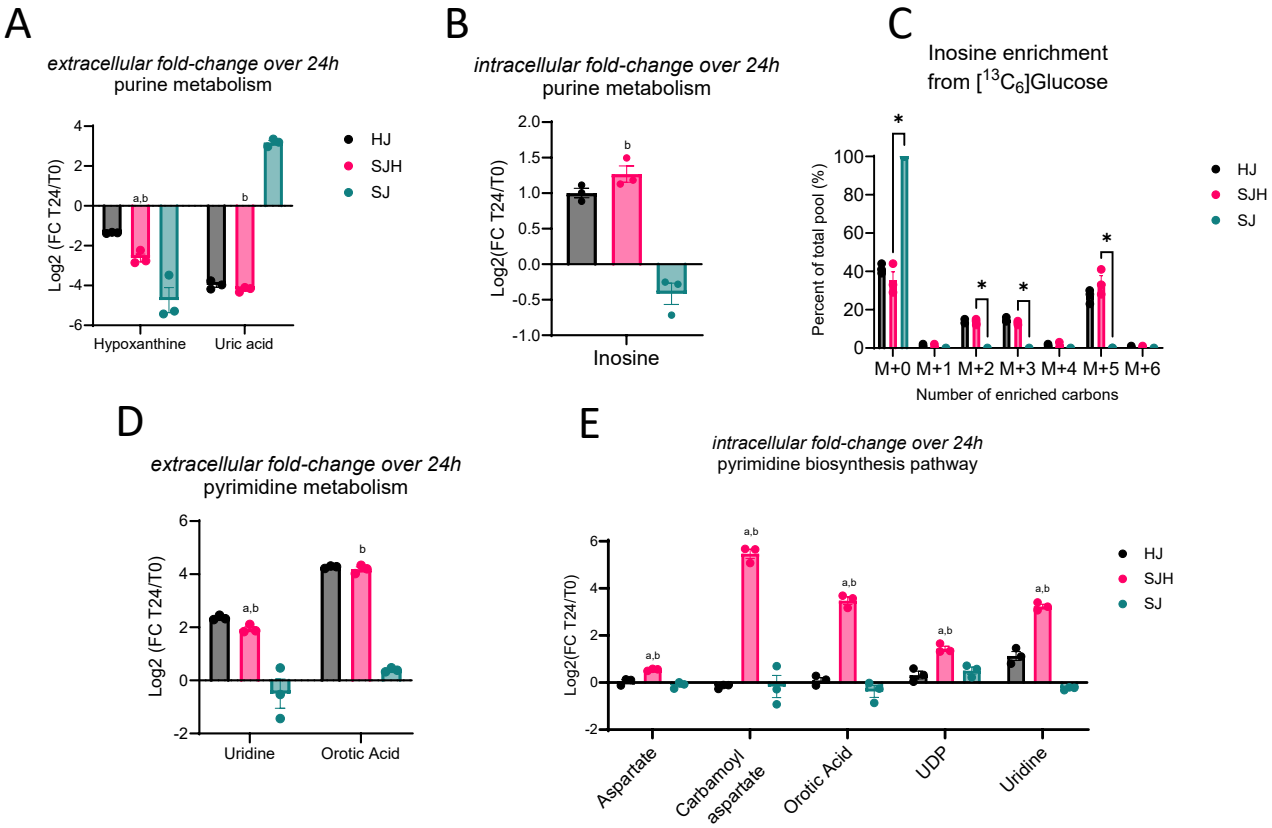
A
extracellular fold-change over 24h
purine metabolism
Log2 (FC T24/T0)
4
2
0
-2
-4
-6
a,b
b
Hypoxanthine
Uric acid
HJ
SJH
SJ
B
intracellular fold-change over 24h
purine metabolism
Log2(FC T24/T0)
2.0
1.5
1.0
0.5
0.0
-0.5
-1.0
b
Inosine
C
Inosine enrichment
from [13C6]Glucose
Percent of total pool (%)
100
80
60
40
20
0
*
*
*
*
M+0
M+1
M+2
M+3
M+4
M+5
M+6
Number of enriched carbons
HJ
SJH
SJ
D
extracellular fold-change over 24h
pyrimidine metabolism
Log2 (FC T24/T0)
6
4
2
0
-2
a,b
b
Uridine
Orotic Acid
E
intracellular fold-change over 24h
pyrimidine biosynthesis pathway
Log2(FC T24/T0)
6
4
2
0
-2
a,b
a,b
a,b
a,b
a,b
Aspartate
Carbamoyl aspartate
Orotic Acid
UDP
Uridine
HJ
SJH
SJ

Figure 5

A

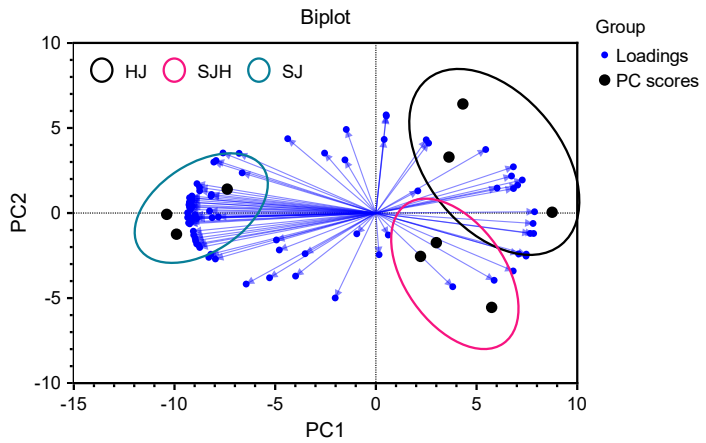
Biplot
Group
Loadings
PC scores
HJ
SJH
SJ
PC2
PC1
10
5
0
-5
-10
-15
-10
-5
0
5
10

B

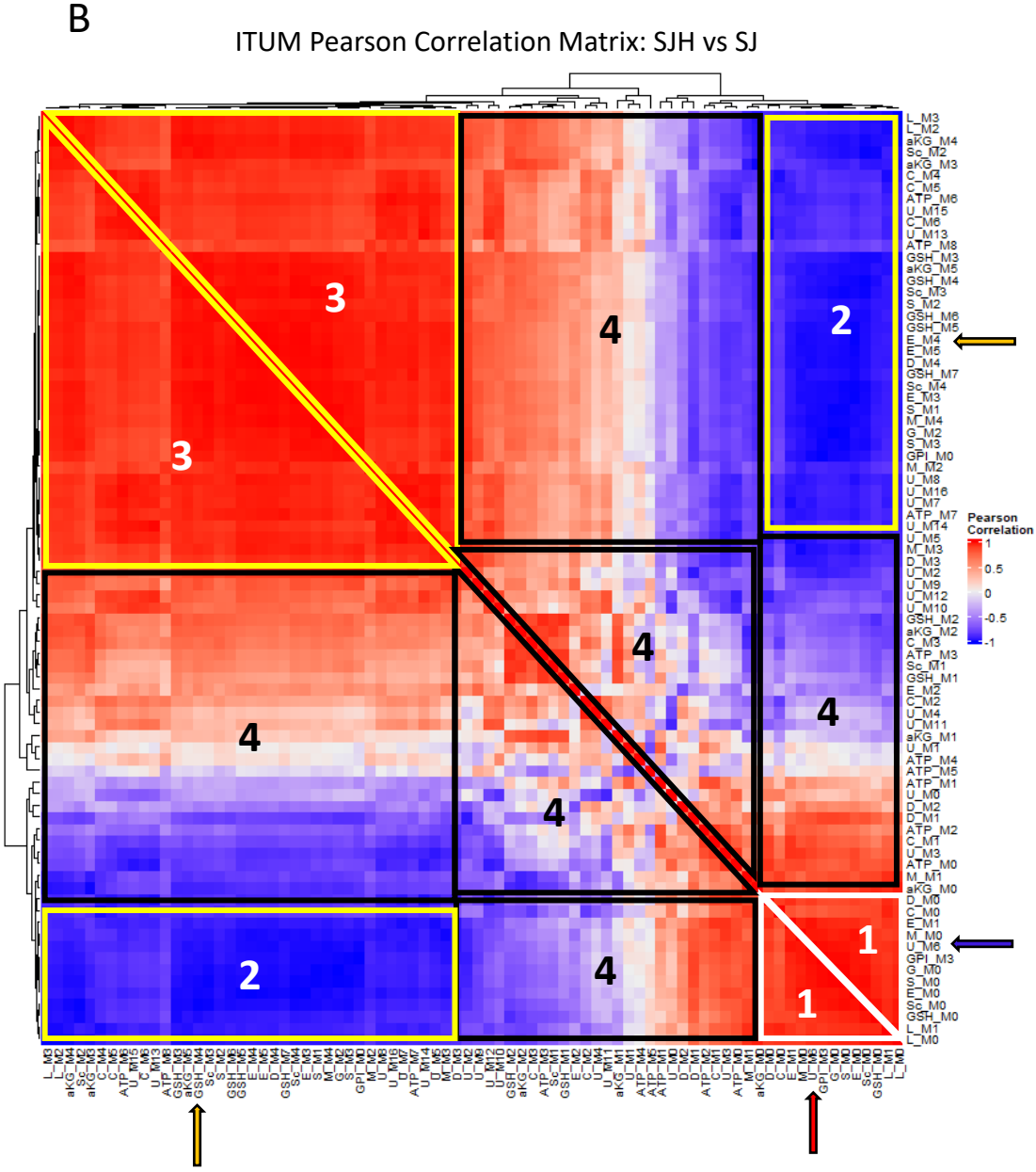
ITUM Pearson Correlation Matrix: SJH vs SJ
Pearson Correlation
1
0.5
0
-0.5
-1
1
2
3
4

Figure 6

A

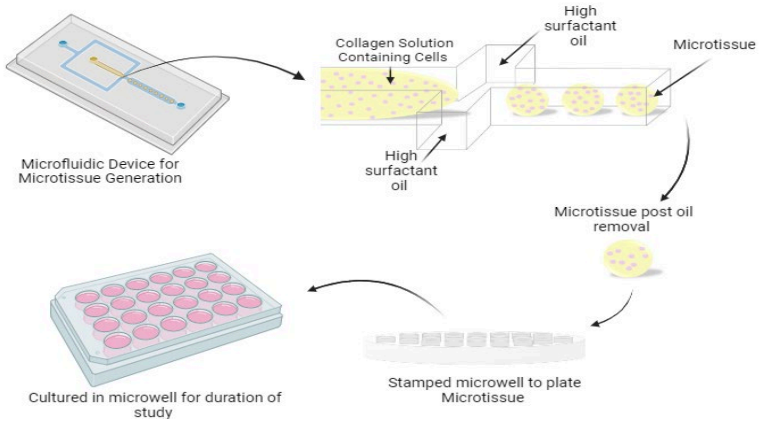

B

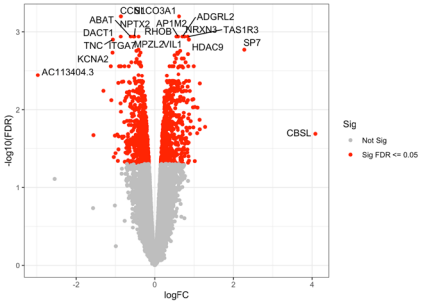

C

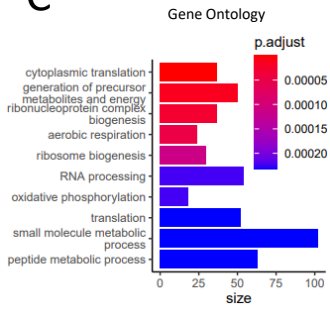

D

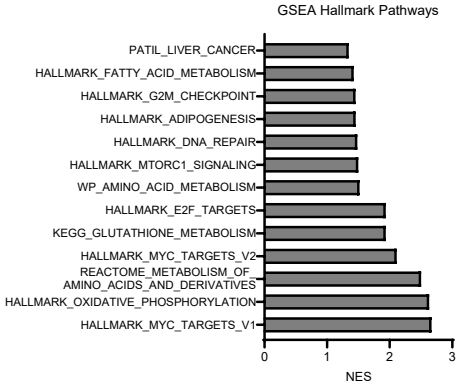

E

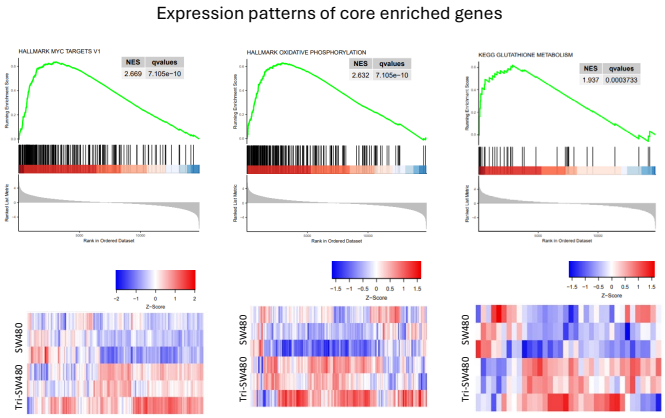

F

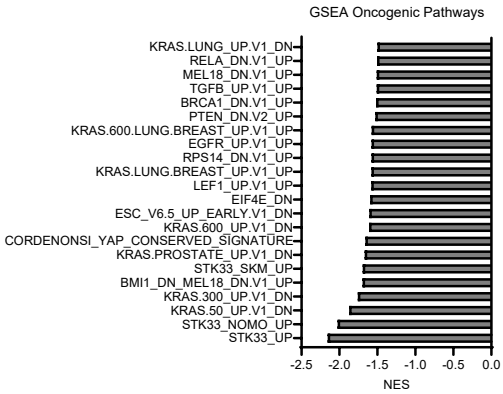

Figure 7

A

Metabolite-Gene Correlation Network

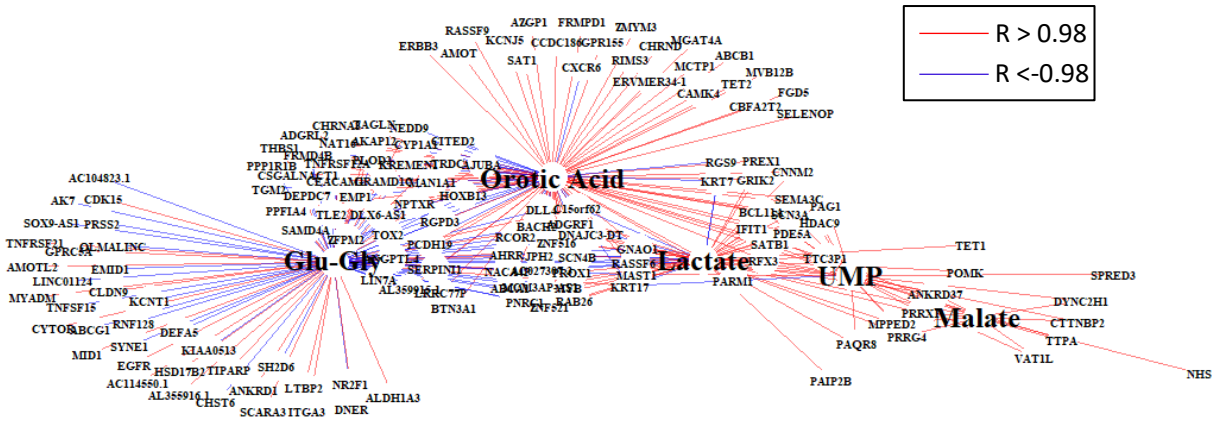

B

Correlation Matrix
Glu-Gly:Transcript Network

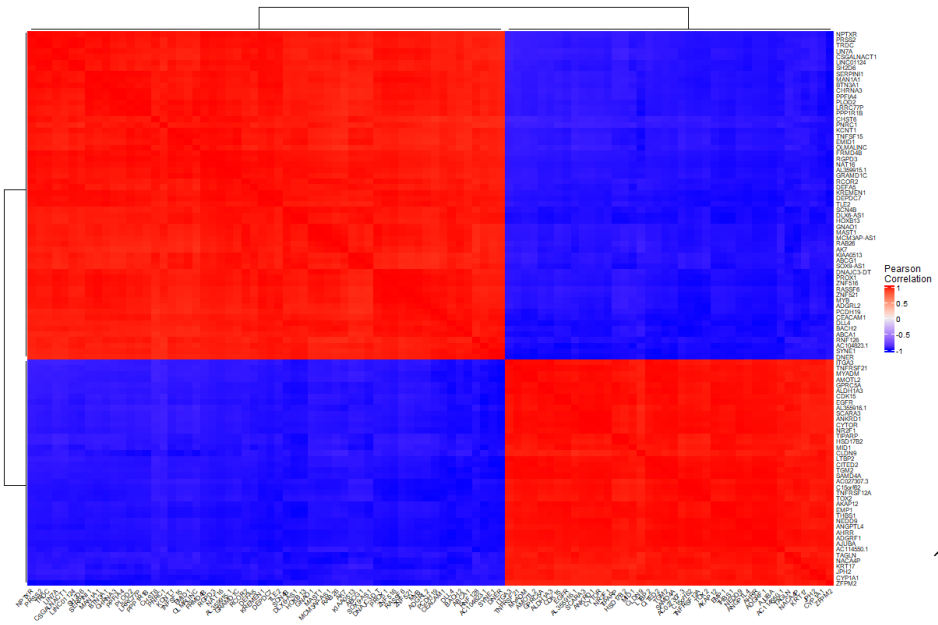

C

GO: Biological Process
Glu-Gly:Transcript Correlation Network

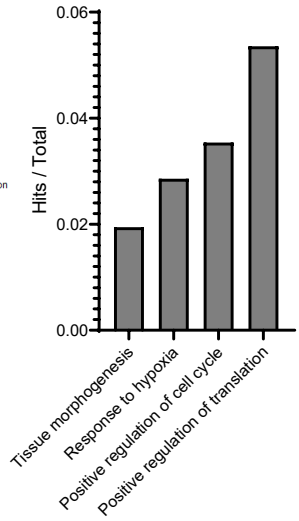

Supplemental Figure 1

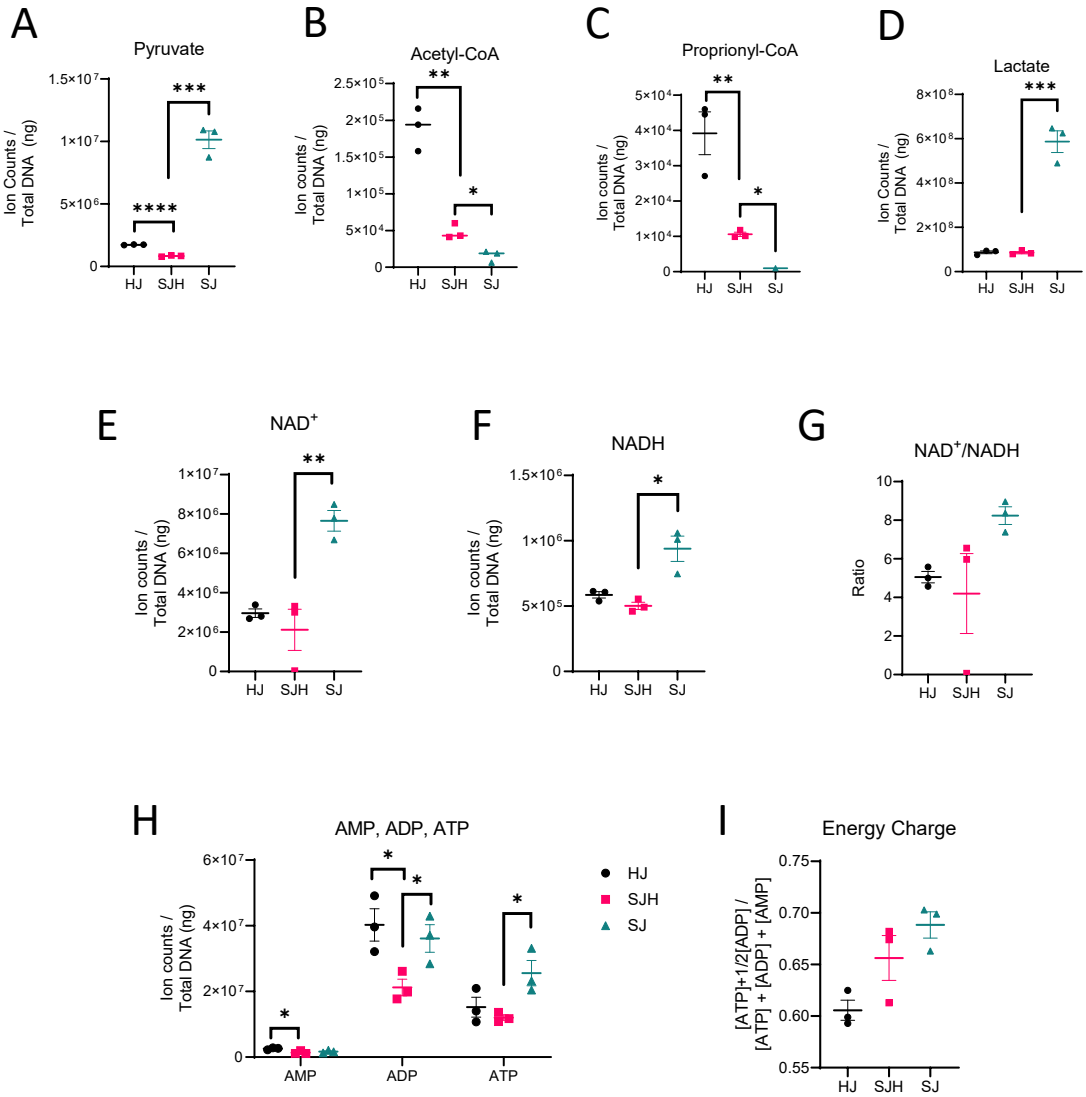

Supplemental Figure 2

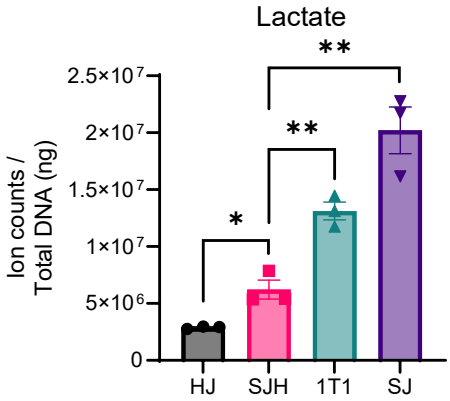

Supplemental Figure 3

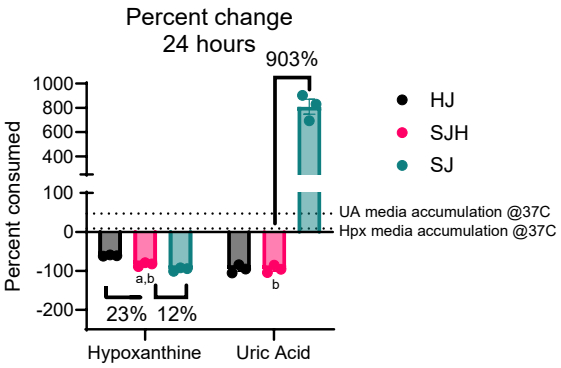

Supplemental Figure 4

ITUM Pearson Correlation Matrix: SJH vs HJ

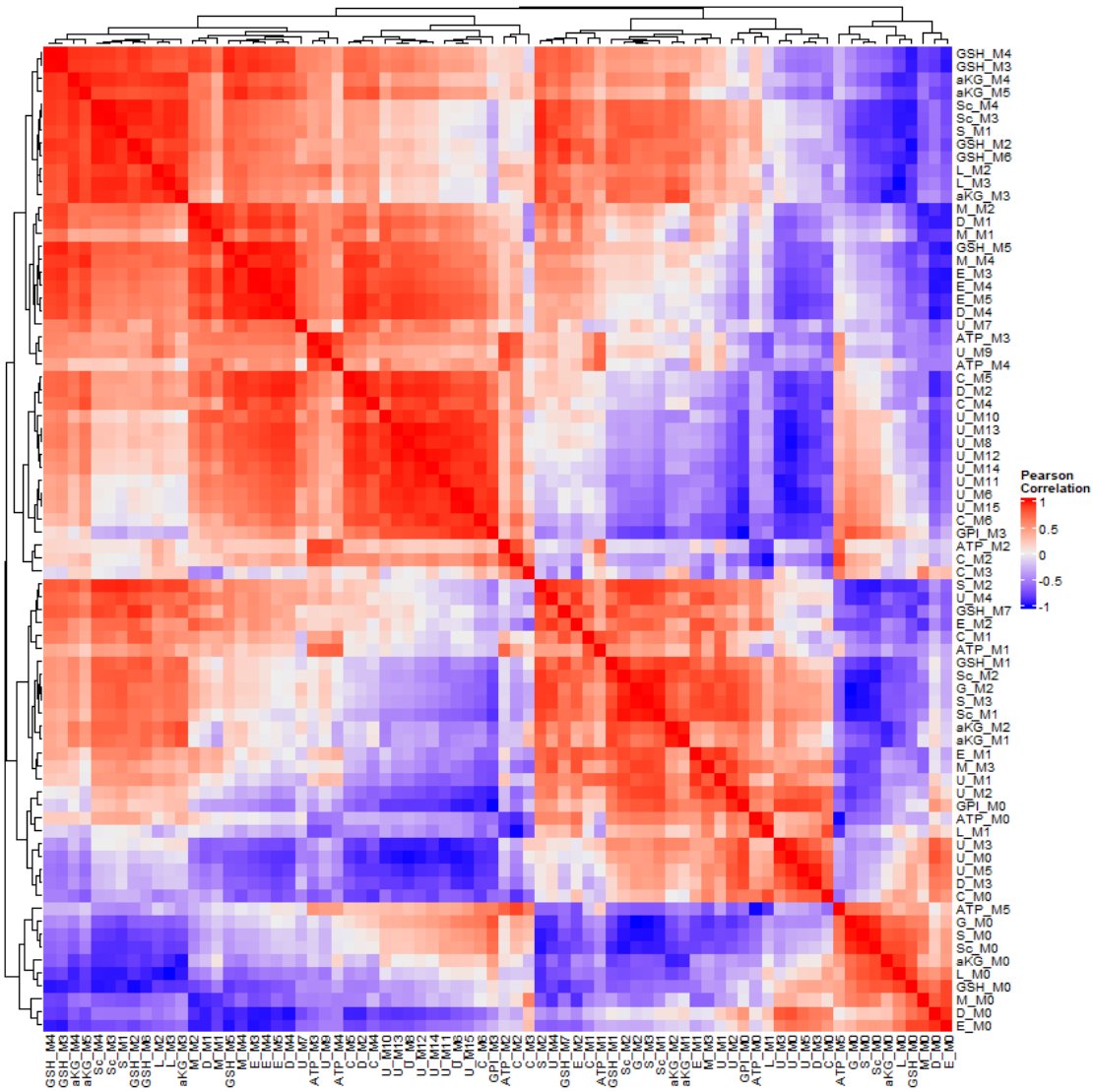

Supplemental Figure 5

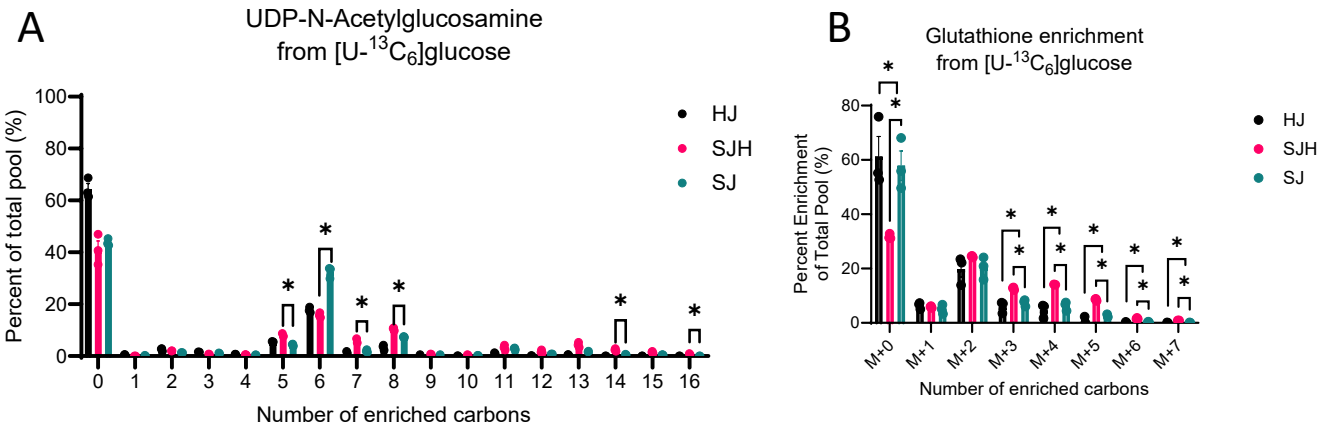

Supplemental Figure 6

A

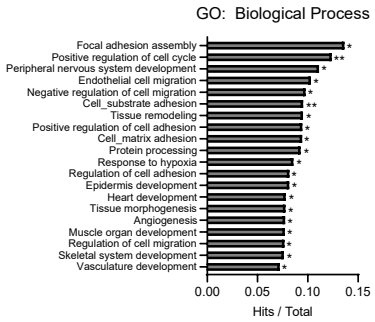
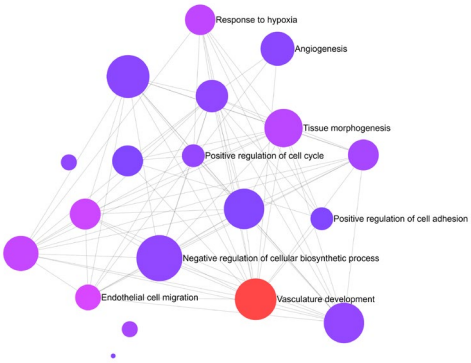
B